2015

Droplet impact on liquid pools: secondary droplets formation from Rayleigh jet break-up and crown splash

Eduardo Castillo Orozco
University of Central Florida

DROPLET IMPACT ON DEEP LIQUID POOLS: SECONDARY DROPLETS FORMATION FROM RAYLEIGH JET BREAK-UP AND CROWN SPLASH

by

EDUARDO A. CASTILLO OROZCO
B.S. Escuela Superior Politécnica del Litoral, 2012

A dissertation submitted in partial fulfillment of the requirements
for the degree of Master of Science in Mechanical Engineering
in the Department of Mechanical and Aerospace Engineering
in the College of Engineering and Computer Science
at the University of Central Florida
Orlando, Florida

Fall-Term
2015

Major Professor: Ranganathan Kumar

ABSTRACT

This work aims to study the impact of a droplet on liquid pools of the same fluid to understand the formation of secondary drops from the central jet and crown splash that occur after the impact. The impact of droplets on a deep pool has applications in cleaning up oil spill, spray cooling, painting, inkjet printing and forensic analysis, relying on the changes in properties such as viscosity, interfacial tension and density. Despite the exhaustive research on different aspects of droplet impact, it is not clear how liquid properties can affect the instabilities leading to the Rayleigh jet breakup and the number of secondary drops formed after it pinches off. In this work, through systematic experiments, the droplet impact phenomena is investigated by varying viscosity and surface tension of liquids as well as impact speeds. Further, using a Volume-of-Fluid (VOF) method, it is shown that Rayleigh-Plateau instability is influenced by these parameters, and capillary timescale is the appropriate scale to normalize the breakup time. Increase in impact velocity increases the height of the thin column of fluid that emerges from the liquid pool. Under certain fluid conditions, the dissipation of this extra kinetic energy along with the surface tension forces produces instabilities at the neck of the jet. This could result in jet breakup and formation of secondary drops. In other words, both the formation of the jet and its breakup require a balance between viscous, capillary and surface tension forces. Based on Ohnesorge number (Oh) and impact Weber number (We), a regime map for no breakup, Rayleigh jet breakup, and crown splash is suggested for $0.0033 \leq Oh \leq 0.136$. For Weber numbers beyond the critical value and $Oh \leq 0.091$ the jet breakup occurs (Rayleigh jet breakup regime). While for $Oh > 0.091$, the jet

breakup is suppressed regardless of the Weber number. In addition, high impact velocity initiates the crown formation and if further intensified it can disintegrate it into numerous secondary drops (crown splash) and it is observed to occur at all Ohnesorge numbers and high enough Weber numbers, however, at high *Oh*, a large portion of kinetic energy is dissipated, thus Rayleigh jet breakup is suppressed regardless of the magnitude of the impact velocity. Moreover, a correlation is proposed for normalized time with respect to the normalized maximum height of jet.

To my wife and our daughter Maria Valentina.

ACKNOLEDGMENTS

I first would like to express my sincere gratitude to my advisor, Dr. Ranganathan Kumar, for placing trust in me, for helping me to improve my research skills, and for his guidance throughout this work.

I would like to thank my lab mates and friends, especially Ashkan Davanlou, Pretam Choudhury, and Carlos Velez for their productive discussions and help to accomplish this work.

I would also like to thank my wife, Marjorie, for her unconditional support during these two years of graduate studies at UCF. Without her encouragement this thesis would not have been possible.

Finally, I wish to acknowledge the American Physical Society for the use of a portion of the article: " E. Castillo-Orozco, A. Davanlou, P. Choudhury, and R. Kumar, Droplet impact on deep liquid pools: Rayleigh jet to formation of secondary droplets, Phys. Rev. E, 2015 " in this thesis.

.

TABLE OF CONTENTS

LIST OF FIGURES

LIST OF TABLES

CHAPTER 1: INTRODUCTION

The droplet impact has been a topic of vast interest over time. Many researchers have studied this phenomenon, enabling us today to have a good understanding. However, there are still many open-ended questions. The purpose of this work is to establish under what circumstances the Rayleigh jet (also known as Worthington jet) breaks up, allowing the formation of subsequent secondary (daughter) droplets, and when the crown splashes from the impact of a liquid drop on a deep pool of the same fluid, as well as to investigate the influence of physical properties of the fluids and impact velocity.

The impact of a droplet may be classified according to the variety of target surface such as dry solid surface, thin liquid film, and deep liquid pool. Many variables determine the outcome of a droplet impact phenomenon, such as the drop size; the physical properties of the liquid such as density, viscosity, and surface tension; and the impact velocity. The present study focuses on droplet impact on deep liquid pool only.

The study of droplet impact on deep liquid pool is important in the analysis of immiscible raindrop on oil slick, having application in cleaning up oil spill. Additionally it has applications in spray cooling and painting, inkjet printing, droplet manipulation, agriculture, etc. Figure 1-1 shows some common applications of droplet impact on deep liquid pools.

There have been diverse studies that investigate the outcomes of droplet impact on solid surface and thin films, which will be reviewed in chapter II. Despite the exhaustive research on different aspects of droplet impact, it is not clear how liquid

properties can affect the instabilities leading to Rayleigh jet break-up and number of secondary droplets formed after its pinch-off. In this thesis, through systematic experimentation, the droplet impact on deep liquid pool is investigated by varying viscosity, surface tension of liquids and the impact velocity of the droplet. To gain insight into the Rayleigh jet phenomenon, a numerical model is developed.

To accomplish the objective of this thesis, experiments are conducted where the release height of the droplet is varied to generate a range of impact velocities. This allows for a large range of Weber number extending up to 1400. In order to investigate the influence of fluid properties such as viscosity, surface tension and density, a wide range of fluids are tested, resulting in Ohnesorge numbers in the range 0.0033 to 0.136 ($0.0033 \leq Oh \leq 0.136$). These experiments are complemented with two-dimensional axisymmetric simulations based on the Volume of Fluid (VOF) and Continuum Surface Force (CSF) methods. The combination of experimental and numerical studies is used to determine the critical Weber number at which the jet pinches off and secondary droplet formation takes place. These models are not only validated by the experiments, but they also serve the role of understanding the Rayleigh-Plateau instability in jet break-up through the pressure and velocity fields at the neck during stretching of the Rayleigh jet.

In this thesis a literature review of the most relevant topics and research on droplet impact is presented in Chapter 2. The experimental procedure and set-up used to get the data for analysis is explained in Chapter 3. The numerical modeling performed for comparison to the experimental data and analysis of this phenomenon is introduced in Chapter 4. The results, along with the physics behind Rayleigh jet formation and beak-up

are discussed in Chapter 5. Finally, conclusion of the entire denouement observed in the previous sections is exhibited in Chapter 7.

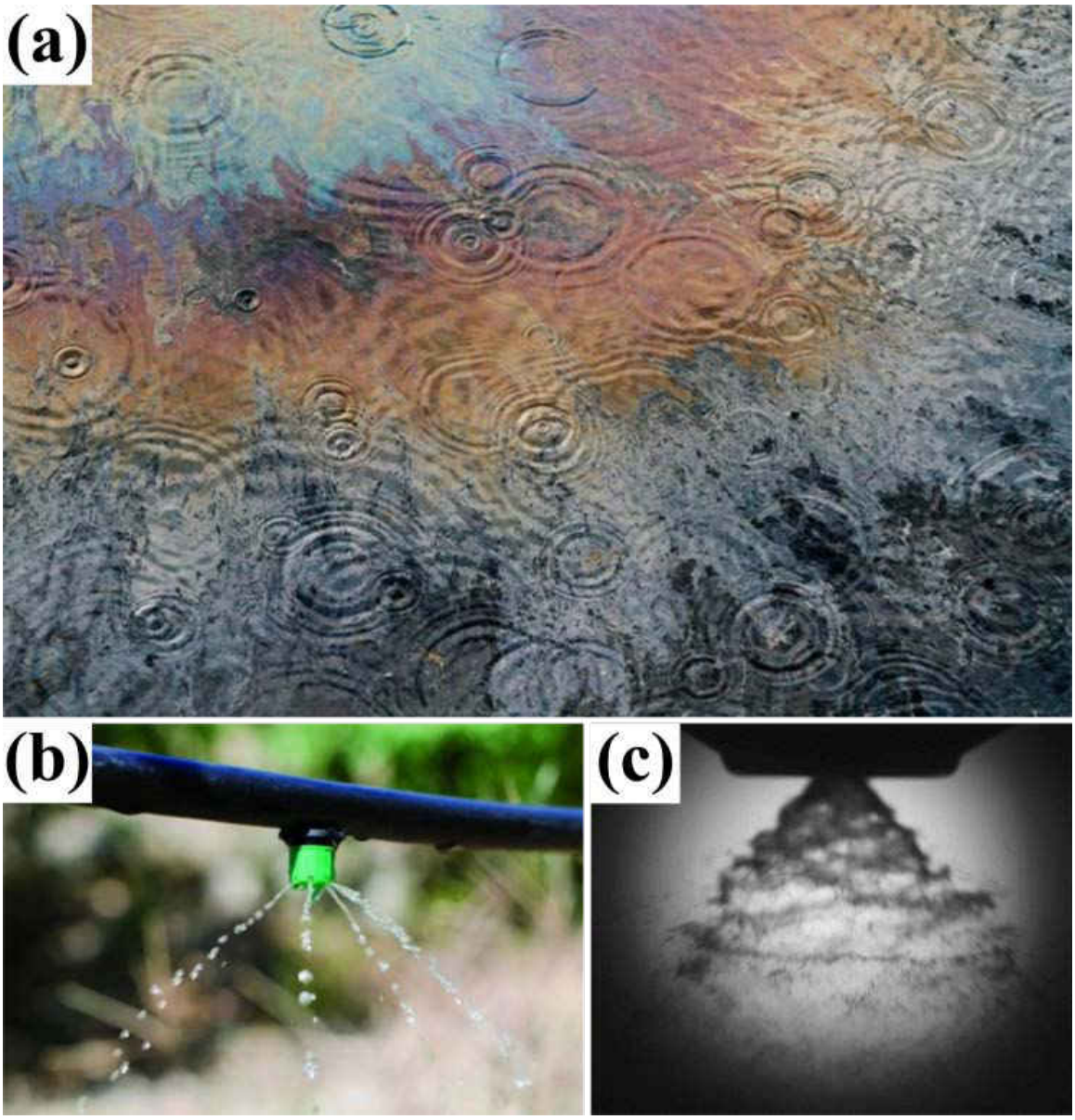

Figure 1-1: (a) Rain falls on oil sheen on the surface of the Gulf of Mexico near the site of the Deepwater Horizon oil well leak in 2010 (Photo source: Patrick Semansky Associate Press). (b) Drip irrigation (adapted from Agroquimica sostenible, http://agroquimica.es). (c) Spray atomization (applicable to spray cooling systems and spray painting).

CHAPTER 2: LITERATURE REVIEW

This section will cover a synopsis of droplet impact studies carried out throughout history until today and an overview of the most relevant subjects related to droplet impact on liquid pools.

O. Reynolds [1] was the first to report that droplets falling gently onto a pool of water would sometimes come to rest on the surface and float there for a few seconds before suddenly coalescing into the pool. Based on these observations he wrote the article "On the action of rain to calm the sea" (Fig. 2-1). In 1908 A.M. Worthington [2] wrote the book "A study of splashes", where he looked into the splash and crater formation upon droplet impact. He applied flash photography to the first consistent study of droplet impact (Fig. 2-2). The droplet impact studies can be classified according to the type of target surface such as dry solid surface, thin liquid film and deep liquid pool.

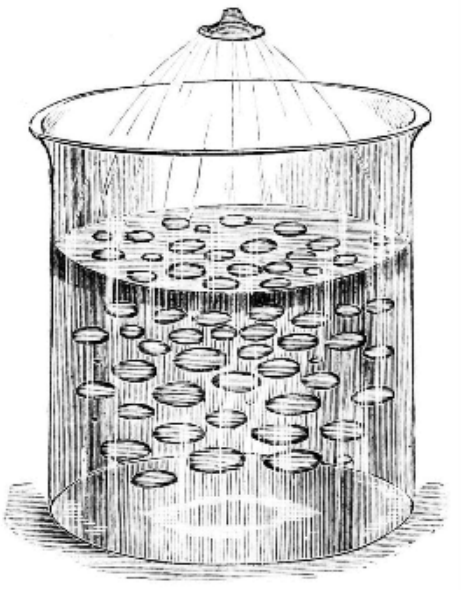

Figure 2-1: Drops descending below the surface –figure reproduced from [1].

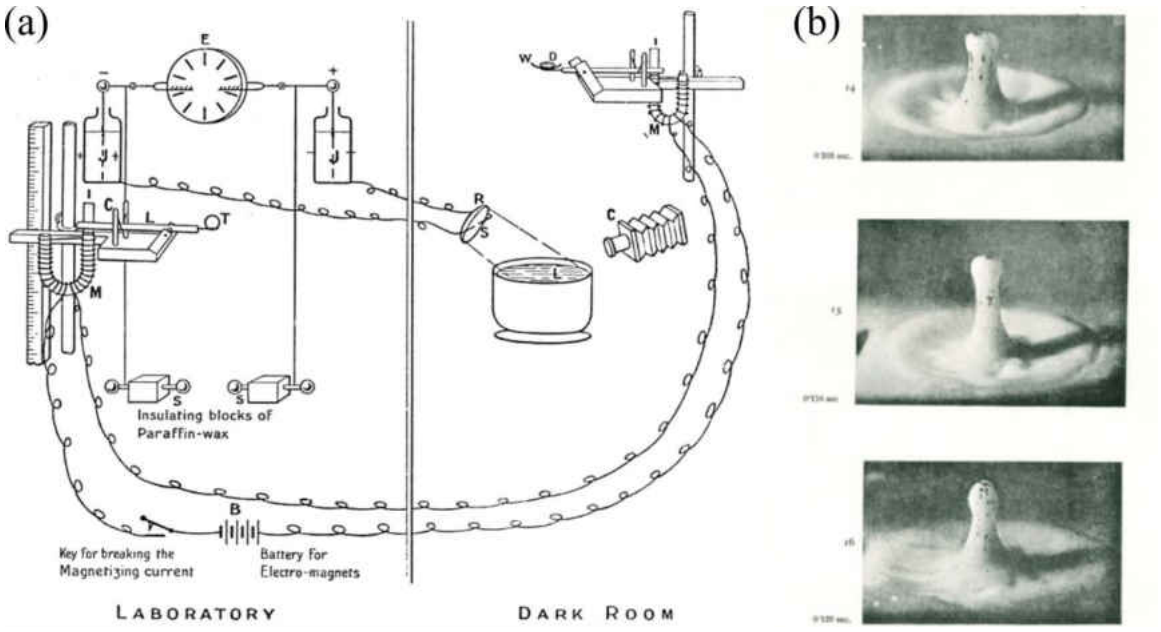

Figure 2-2: (a) Arrangement of apparatus for photographing splashes. (b) Rayleigh jet photographs at different times – figure reproduced from [2].

M. Rein [3] studied the fluid dynamics of drop impact. He observed bouncing, spreading and splashing on solid surfaces, and bouncing, coalescence and splashing on liquid surfaces, as well as occasionally cavitation and entrainment of gas into the impacted liquid. Rioboo et al. [4] carried out a qualitative analysis of the various outcomes of a drop impact on solid surface with different roughness and wettability. They found that there are at least six distinct outcomes of a drop impact on a solid surface, which are deposition, prompt splash, corona splash, receding break-up, partial rebound, and rebound. Clanet et al. [5] studied the impact of a liquid drop of low viscosity (such as water) on a super-hydrophobic surface. They proposed that the maximal spreading D_{max} scales as $D_o We^{1/4}$, where D_o is the droplet diameter and We is the Weber number. Manzello and Yang [6] conducted experiments for water impingement on

a liquid surface. They covered a range of impact Weber number of 5.5 to 206. Pan and Law [7] investigated the head-on collision of a droplet on a liquid layer (thin film) of the same material; they focused on the transition from bouncing of the droplet to its absorption by the film. Their experimental results showed that absorption is favored with increasing droplet Weber number, *We*. Zhang et al. [8] studied the crown splash originated from the impact of a drop onto a thin liquid film. They suggested that for a range of parameters in the crown splash regime, the origin of secondary droplets results from Rayleigh-Plateau instability of the rim. Banks et al. [9] found crown formation thresholds for drop impacts onto thin films. They considered the effect of drop and film viscosity on this study. Tran et al. [10] investigated the air entrainment during impact of droplet on a deep pool. They reported the dependence of the rupture position of the trapped air layer under the droplet, on the liquid viscosity and the impact velocity. Agbaglah et al. [11] studied droplet impact into a deep pool. They used high-speed X-ray imaging method to show that vortex separation within the drop leads to the formation of a second jet long after the formation of the ejecta sheet. Some of the most general aspects encompassed in droplet impact can be found in the review by Prosperetti and Oğuz [12].

When a drop impinges on a bath of the same fluid, depending on the impact velocity *U*, a full or partial coalescence may occur. Full coalescence is known as the case where the drop fully merges with the interface. Partial coalescence is a more complex phenomenon, in which the merging does not complete; instead a secondary droplet is left behind. Mohamed-Kassim and Longmire [13] employed current optical methods such as high-speed imaging and particle image velocimetry (PIV) to study the rupture and coalescence of a drop through the liquid interface. They obtained continuously evolving

velocity fields within the drop and the surrounding liquids before and after the drop rupture. X. Chen et al. [14] did a study on partial coalescence; they found an intermediate range of drop sizes in which the merger is not complete but a secondary droplet was formed, and, that for drops that were too large or too small, partial coalescence was arrested by gravity or viscosity, respectively. Blanchette and Bigioni [15] proposed a criterion for partial coalescence based on Bond number, *Bo,* and Ohnesorge number, *Oh*.

$$Bo = \frac{\Delta \rho g R^2}{\sigma} \quad (1)$$

$$Oh = \frac{\mu}{\sqrt{\sigma \rho R}} \quad (2)$$

where μ, σ and ρ are the dynamic viscosity, surface tension and density of the liquids, g is the gravitational constant, and R is the radius of initial droplet. They suggested that pinch-off mechanism depends on the early dynamics of coalescence rather than Rayleigh-Plateau instability. It is important to notice that the effect of impact velocity was not considered by Blanchette and Bigioni as liquid drops were deposited gently onto the surface of the liquid, so that the kinetic energy was low. Gilet et al. [16] studied the partial coalesce of droplet on a liquid-liquid interface by tuning the viscosities of both liquids. They investigated the ratio between the secondary droplet size and the mother droplet size as a function of Bond number, Ohnesorge number, and the density relative difference, as well as the propagation and damping of the wave's convergence on the top of the droplet, and suggested that additional to Blanchette and Bigioni's considerations, other viscous mechanisms have been suspected to enhance or to avoid partial coalescence. Blanchette et al. [17] examined the influence of surface tension gradients on the coalescence of a drop with a liquid reservoir of a miscible but distinct fluid. They

found three regimes, depending on the reservoir to drop surface tension ratio. Thoroddsen and Takehara [18] suggested that the surface tension time scale can be used to scale the time associated with partial coalescence and that the cascade of a drop is limited due to viscous effects. Aryafar and Kavehpour [19] studied droplet coalescence at a planar fluid-fluid interface in the Stokes regime. They reported a hydrodynamic instability at the rim of the interfacial bridge that formed between the drop and the interface.

For partial coalescence, there is lack of literature, nevertheless, it is popularly agreed that ratios of gravity to surface tension force (Bond number, *Bo*), inertia to viscous forces (Reynolds number, *Re*), inertia to surface tension (Weber number, *We*) and viscosity to surface tension (Ohnesorge number, *Oh*) are the main parameters that play an important role in determining the dynamics of instability on the liquid surface due to droplet impact. In spite of this knowledge, results for a wide range of these parameters are not generally available to date.

$$Re = \frac{\rho U R}{\mu} \quad (3)$$

$$We = \frac{\rho U^2 R}{\sigma} \quad (4)$$

Contemporary studies related to the formation of secondary drops have been accomplished by others. Deegan et al. [20] looked into the distinct dynamical origins of the secondary droplets. They developed a regime map based on *We* and *Re* for crown splash (instability in Peregrine sheet that leads to large droplets) and found a power law relationship between those two numbers. Hoepffner and Paré [21] showed that the vortex rings created by viscous shear in the jet could delay the pinch-off and recoil as a liquid filament. Ghabache et al. [22] investigated the jet produced by bubble bursting, focusing

on the influence of viscosity and gravity. They correlated the initial shape and aspect ratio of the cavity to the height and thickness of the jet in bubble bursting. Walls et al. [23] focused on the special case when both gravitational and viscous effects are important in jet-drop formation as in sea slicks and metalworking fluid. In their work, air was injected into the bottom of a water-glycerol solution.

Beside experimental works, numerical studies have been also used for investigation of the droplet impact phenomena. Rieber and Frohn [24] solved the Navier-Stokes equations directly to capture the dynamics of splashing by simulating the impact of a single drop on a liquid film. In their work, Rayleigh instability is introduced as the dominant mechanism for cusp formation. Gupta and Kumar [25] employed a two dimensional lattice Boltzmann model to simulate droplet impingement on a dry surface. They established multiple phases that lead to break-up, for cases of low density ratio liquids. Berberović et al. [26] used volume of fluid method to detect the penetration far from the wall at early times after the impact of a drop on a liquid film. They analyzed the shape of the cavity due to droplet impact, the formation and propagation of a capillary wave in the crater, and the residual film thickness on the wall. Chen and Guo [27] employed volume of fluid in conjunction with the continuum surface force (CSF) model to investigate the viscosity effect on regular bubble entrapment during drop impact on a deep pool. Ray et al. [28] simulated the impact of a water drop on water to study gas bubble entrapment and jet formation. They developed regime maps, based on Weber number (We = 50 to 300), and Froude number (Fr = 25 to 600).

CHAPTER 3: EXPERIMENTAL SETUP

Figure 3-1 shows the schematic of the experimental setup. A circular transparent petri dish with a diameter of 80 mm and thickness of 13 mm was used as the container. The container is large enough to minimize the wall effect. Drops were generated using a syringe pump (World Precision Instruments) at a flow rate of 100 µL/min, using a needle with a nominal outer diameter of 0.64 mm (hypodermic needle gauge 23. A high-speed camera (i-Speed 2, Olympus) connected to a zoom lens (Navitar) captured the events at 2000 frames per second with a resolution of 576 x 432 pixels. The images were extracted from the videos and analyzed using a MATLAB code (included in Appendix A). The minimum resolution and maximum uncertainty of the measurements from the imaging were 0.06 mm (1 pixel) and 0.126 mm respectively. The illumination was provided by a 1000-watt halogen lamp. The camera was set to capture the interface and droplet from the side. The heat generation caused by illumination was controlled to avoid thermal gradient between the two media [29,30]. The properties of different liquids along with the droplet diameter, D_o, used in the experiment are presented in Table 3-1. All the experiments were carried out at room temperature of 24.6°C +/-1°C, and were repeated at least three times to assure repeatability of the data.

Droplets were generated using a syringe pump, needle and plastic tubing. The release height was controlled using a 1D stage which had millimeter size precision. The release height was varied (0.1 m - 2.5 m) in order to generate a rage of impact velocities. The size of droplets was consistent for a given fluid as the gravitational force overcomes the capillary force. After each test, the syringe, tubing and container were changed.

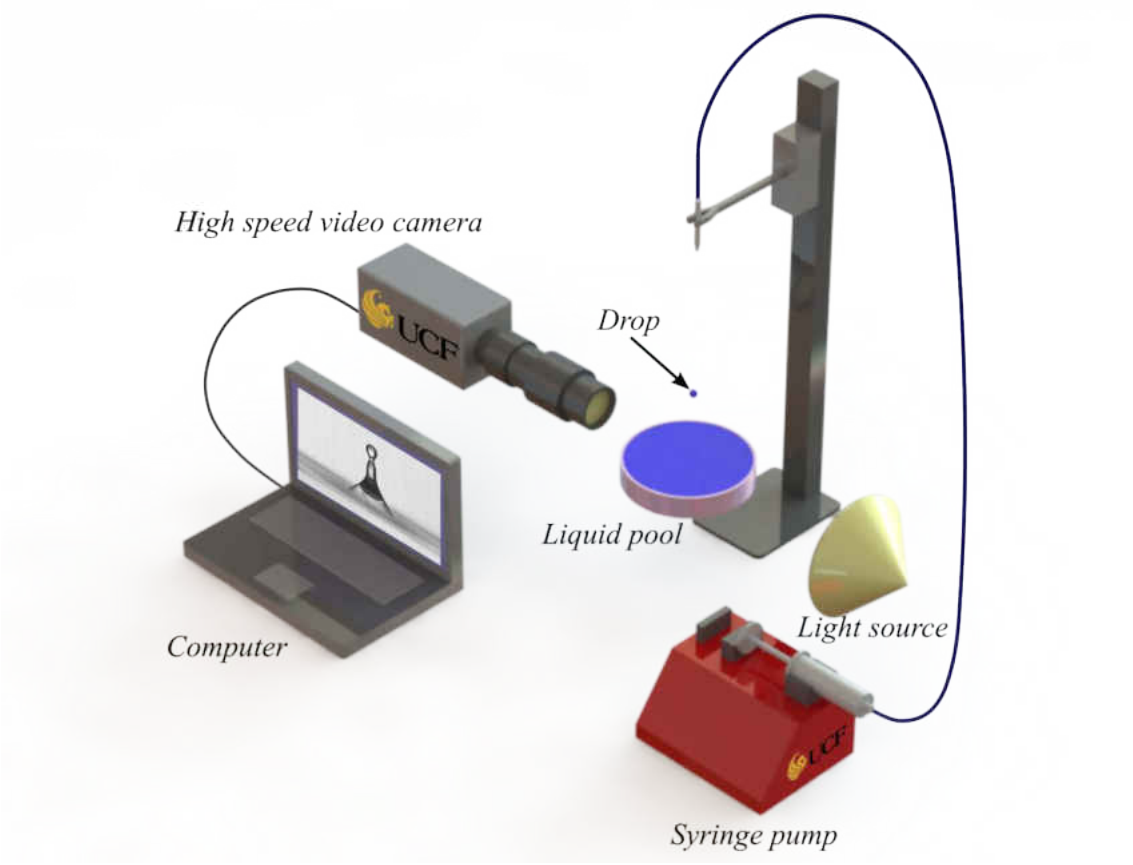

Figure 3-1: Experimental set-up.

Table 3-1: Physical properties of tested liquids at room temperature.

Liquids	D_o (mm)	ν (cSt)	ρ (g/cm^3)	σ (mN/m)	Oh
Water	2.50	1.0	1.0	72.0	0.0033
Potassium hydroxide	2.70	1.05	1.0	72.1	0.0033
Ethanol	1.93	1.4	0.79	22.0	0.0085
Ethylene glycol	2.20	17.8	1.1	47.7	0.0815
Silicone oil 5 cSt	1.80	5.0	0.91	19.7	0.0360
Silicone oil 10 cSt	1.80	10.0	0.93	20.1	0.0716
Silicone oil 13 cSt	1.90	13.0	0.94	20.2	0.0907
Silicone oil 14 cSt	1.90	14.0	0.94	20.3	0.0952
Silicone oil 16 cSt	1.96	16.0	0.94	20.4	0.1087
Silicone oil 18 cSt	1.98	18.0	0.95	20.5	0.1222
Silicone oil 20 cSt	2.0	20.0	0.95	20.6	0.1358

CHAPTER 4: NUMERICAL FORMULATION

4.1 Numerical Model and Governing Equations

The volume of fluid method (VOF) is used in combination with the continuum surface force model (CSF) and implemented in the open-source platform, OpenFOAM [31]. OpenFOAM utilizes a cell center based finite volume method on the grid. Specifically, the InterFoam solver is employed to perform the numerical simulation of the droplet impact process. The pressure implicit with splitting of operators (PISO) algorithm [32] is used as the solution procedure for coupling between pressure and velocity in transient flow.

VOF method considers two different phases as one fluid in the entire domain, where the phases within the domain are tracked by variable γ that is based on the volume fraction (Hirt and Nichols, [33]). The volume fraction takes on values between 0 and 1.Then the physical properties of the mixture are defined using volume fraction as follows:

$$\rho = \gamma\rho_l + (1-\gamma)\rho_g \quad (5)$$

$$\mu = \gamma\mu_l + (1-\gamma)\mu_g \quad (6)$$

where ρ_g, μ_g are the density and viscosity of the gaseous phase, and ρ_l, μ_l represent the density and viscosity of the liquid phase. When solving the problem in the gaseous phase, the volume fraction is $\gamma = 0$, which makes $\rho = \rho_g$ and $\mu = \mu_g$. When solving in the liquid phase, $\gamma = 1$, $\rho = \rho_l$ and $\mu = \mu_l$. At the interface, γ takes on values between 0 and 1, and the weighted values are used. The physical properties such as density and viscosity are considered constant within each phase, but they vary at the gas-liquid interface.

Equations governing the fluid mechanics of the droplet impact phenomenon are the continuity, momentum, and transport of the volume fraction equation. It must be mentioned that the case studied in this thesis correspond to an unsteady, incompressible, viscous, immiscible two-phase flow problem and that the flow conditions caused by the drop impact on a liquid surface are considered to be laminar and axisymmetric.

The conservation of mass for both fluids (liquid and gas), is described by the continuity equation. The differential form of the continuity equation is shown [34] as follows (Vectors are set in boldface type):

$$\frac{\partial \rho}{\partial t} + \boldsymbol{\nabla} \cdot (\rho \boldsymbol{V}) = 0 \qquad (7)$$

where, $\boldsymbol{V}$ is the velocity field, t is the time, and ρ is the density. Fluids are considered incompressible in this work, thus, Eq. (7) can lead to Eq. (8) for this special case.

$$\boldsymbol{\nabla} \cdot (\rho \boldsymbol{V}) = 0 \qquad (8)$$

The momentum equation with Newton's viscosity law can be expressed [35] as follows:

$$\frac{\partial (\rho \boldsymbol{V})}{\partial t} + \rho(\boldsymbol{V} \cdot \boldsymbol{\nabla})\boldsymbol{V} = -\boldsymbol{\nabla} p + \rho \boldsymbol{g} - \frac{2}{3}\boldsymbol{\nabla}(\mu \boldsymbol{\nabla} \cdot \boldsymbol{V}) + 2\boldsymbol{\nabla} \cdot (\mu \boldsymbol{S}) \qquad (9)$$

Eq. (9) can also be shown in a more compact form (Eq. 10) by using the definition of the deviatoric stress tensor, $\boldsymbol{T}$.

$$\frac{\partial (\rho \boldsymbol{V})}{\partial t} + \rho(\boldsymbol{V} \cdot \boldsymbol{\nabla})\boldsymbol{V} = -\boldsymbol{\nabla} p + \rho \boldsymbol{g} + \boldsymbol{\nabla} \cdot \boldsymbol{T} \qquad (10)$$

where, the deviatoric stress tensor is defined by, $\boldsymbol{T} = -\frac{2}{3}\mu \delta_{ij} \boldsymbol{\nabla} \cdot \boldsymbol{V} + 2\mu \boldsymbol{S}$, the mean rate of strain tensor is $\boldsymbol{S} = 0.5[\boldsymbol{\nabla V} + (\boldsymbol{\nabla V})^T]$, and, δ_{ij} is the Kronecker delta tensor, which is also known as the substitution or the identity tensor. Finally the same momentum

equation, but with the addition of the surface tension force is shown in Eq. (11), where the pressure, viscosity, and gravity are denoted by p, μ, and $\boldsymbol{g}$, respectively. $\boldsymbol{F_\sigma}$ is the surface tension force that is taken into account in the momentum equation .

$$\frac{\partial(\rho \boldsymbol{V})}{\partial t} + \rho(\boldsymbol{V} \cdot \boldsymbol{\nabla})\boldsymbol{V} = -\boldsymbol{\nabla} p + \boldsymbol{\nabla} \cdot (\mu[\boldsymbol{\nabla V} + (\boldsymbol{\nabla V})^T]) + \rho \boldsymbol{g} + \boldsymbol{F_\sigma} \quad (11)$$

The CSF model (Brackbill et al. [36]) is used to evaluate the surface tension force in the momentum equation. The surface tension force is defined by the Eq. (12) as follows:

$$\boldsymbol{F_\sigma} = \sigma k \boldsymbol{\nabla} \gamma \quad (12)$$

where the interfacial tension between phases is σ, and k the interfacial curvature. The term $\boldsymbol{\nabla}\gamma$ acts only at the gas-liquid interface, where volume fraction changes. The interfacial curvature is expressed by the CSF model as Eq. (13).

$$k = -\boldsymbol{\nabla} \cdot \left(\frac{\boldsymbol{\nabla}\gamma}{|\boldsymbol{\nabla}\gamma|}\right) \quad (13)$$

In the conventional VOF method, the transport equation for the volume fraction of one phase is solved simultaneously with the continuity equation (8) and the momentum equation (11), and is defined by Eq. (14) as follows:

$$\frac{\partial(\gamma)}{\partial t} + \boldsymbol{\nabla} \cdot (\boldsymbol{V}\gamma) = 0 \quad (14)$$

In computational fluid dynamics (CFD) solution of this two-phase flow problem, the interface is affected due to numerical diffusion and the discretization of the convective term is of most importance. To maintain the sharp resolution of the interface, Weller [37] added an artificial convective term, which is also known as compression term, $\boldsymbol{\nabla} \cdot (\boldsymbol{V_r}\gamma[1-\gamma])$, into the transport equation of volume fraction. The numerical

diffusion could be limited by adding the additional convective term, while "$\boldsymbol{\nabla}\cdot$" guarantees conservation and "$\gamma(1\text{-}\gamma)$" guarantees boundedness. Therefore the artificial convective term is present only at the interface, where γ takes on values between 0 and 1. Thus, the new transport equation for the volume fraction is shown in Eq. (15) as follows:

$$\frac{\partial(\gamma)}{\partial t} + \boldsymbol{\nabla}\cdot(\boldsymbol{V}\gamma) + \boldsymbol{\nabla}\cdot(\boldsymbol{V_r}\gamma[1-\gamma]) = 0 \qquad (15)$$

where, $\boldsymbol{V_r}$ is the relative velocity at the interface and it was defined by [37] as:

$$\boldsymbol{V_r} = n_f min\left[c_f|\boldsymbol{V}|, max(|\boldsymbol{V}|)\right]\frac{\nabla\gamma}{|\nabla\gamma|} \qquad (16)$$

where, n_f is the unit normal flux on a cell face at the interface region, c_f is the compression constant ($c_f = 1$ for this problem), $|\boldsymbol{V}|$ is obtained by the pressure-velocity coupling algorithm, and $max|\boldsymbol{V}|$ is the largest value of $|\boldsymbol{V}|$ anywhere in the domain.

4.2 Initial and boundary conditions

As mentioned earlier, drop impact followed by secondary drop formation is assumed to be axisymmetric. Note that droplet and liquid pool are both the same liquid and are surrounded by air. The computational domain is shown in Fig. 4-1. The z-axis accounts for symmetry axis in which the gravity force acts. The bottom and right boundaries are walls with no-slip condition, while the top boundary is an open boundary where fluids can flow freely. The domain size is 40 mm x 40 mm. In the beginning of the simulation, the drop and liquid pool are set within the domain by establishing an initial volume fraction. The initial volume fractions in the two phases are: Air: $\gamma = 0$; Liquid: $\gamma = 1$. The capillary pressure difference across the droplet interface is considered as

initial condition. The original droplet is considered spherical and the capillary pressure difference is obtained according to the Young-Laplace equation (Eq. 17). In addition, the static pressure is offset by the hydrostatic pressure $\rho g z$ so that the initial pressure at the walls is 0.

$$\Delta p = \frac{2\sigma}{R_o} \qquad (17)$$

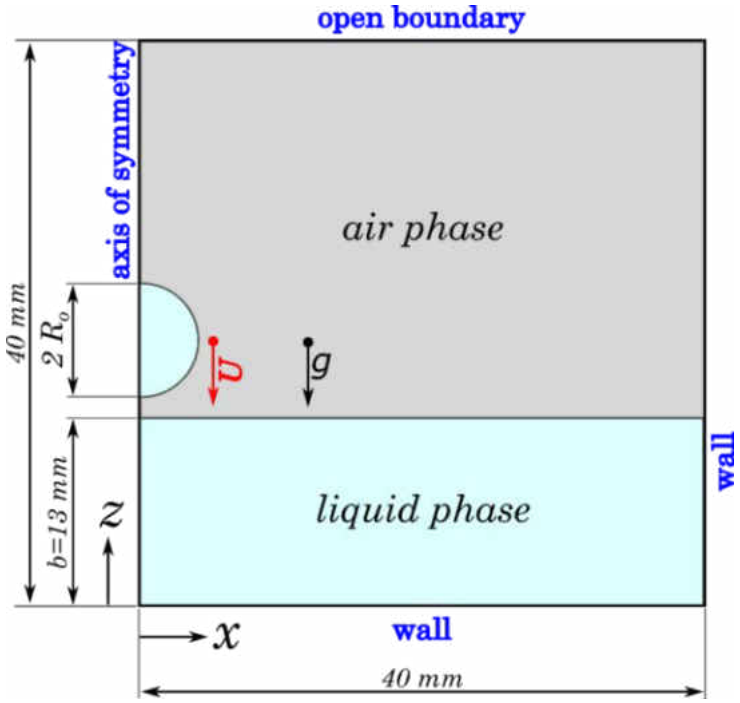

Figure 4-1: Computational domain and boundary conditions for 2D axisymmetric CFD analysis.

4.3 Grid independence

A standard mesh size of 0.16 mm x 0.16 mm is used to create the entire domain, except near the liquid interface where the mesh is refined. Since OpenFOAM does not work with 2D geometries, a wedge of 5° angle is modeled, where the faces on the x-z

plane are set symmetric and only one element is present along the y-axis. Five different mesh types are tested to check for grid independence. The cell sizes used within the refined region are 50 µm x 50 µm, 25 µm x 25 µm, 15 µm x 15 µm, 10 µm x 10 µm, and 5 µm x 5 µm. The computational grid is shown in Fig. 4-2.

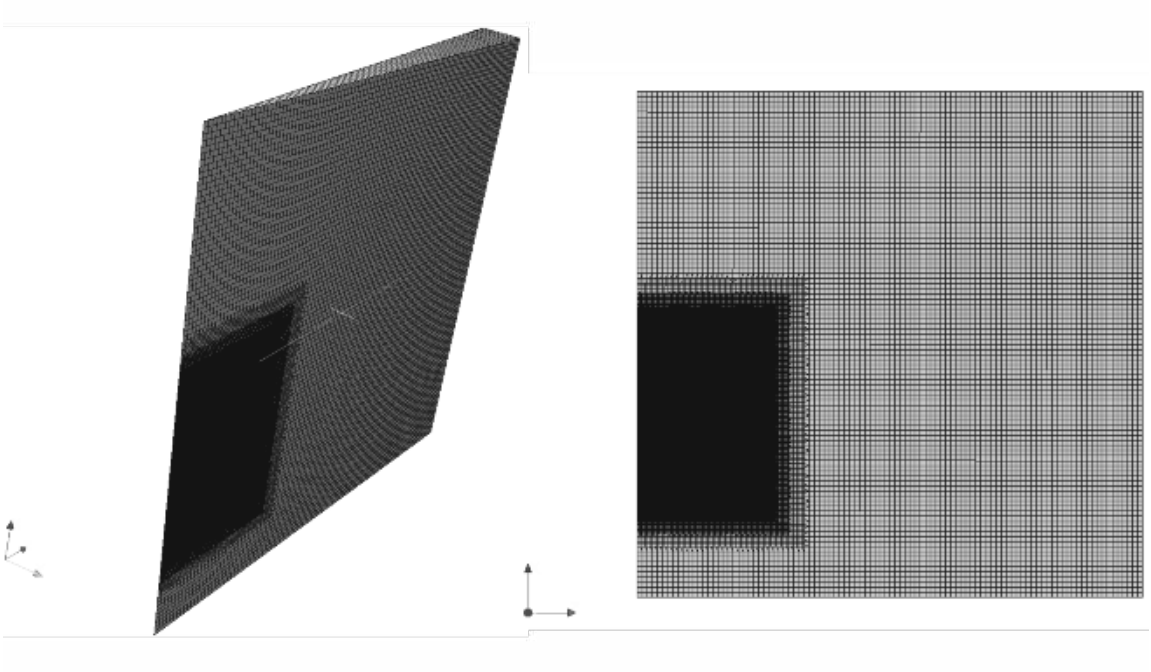

Figure 4-2: Computational grid

The numerical simulation of silicone oil 5 cSt is used to investigate the grid dependence of the solution (D_o = 1.8 mm, U = 1.8 m/s) for We = 135 and Re = 324. In order to evaluate the grid resolution effect, the height of the cylindrical column from droplet impingement up to jet breakup is examined (Fig. 4-3). The crater formation after impact (region A), Rayleigh jet before pinch-off and the recession of the jet back into the pool (region B) as well as the subsequent secondary droplet (region C) are shown in Fig.

4-4a. It is clear that in region A, there is no significant variation in height for all cases. However, in regions B and C, grid independence is achieved for 10 µm x 10 µm, which is selected as the final grid.

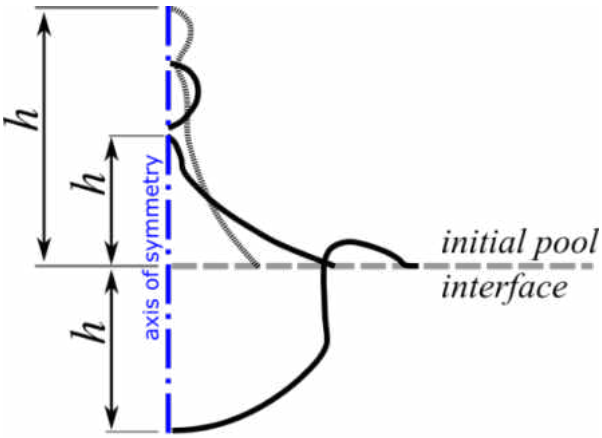

Figure 4-3: Tracking of crater depth and height of jet along axis of symmetry.

4.4 Experimental validation of numerical results

The variation of the height of the cylindrical column up to the pinch-off is compared quantitatively with experimental results in Fig. 4-4b. The experimental result for validation of the numerical simulation is obtained after repeating experiments fifteen times, where the maximum sample standard deviation is S_x = 0.059 mm, which leads to a maximum uncertainty of 0.126 mm at 95% probability (shown as error bars in Fig. 4-4b). The numerical simulations are compared qualitatively with the experimental results in Fig. 4-5, where the secondary drop pinches off after 52.6 ms from the initial droplet impact. The results from the CFD simulation match well with the experimental results. The errors in the maximum height of the jet and secondary droplet diameter are 2.2% and 3.4%, respectively.

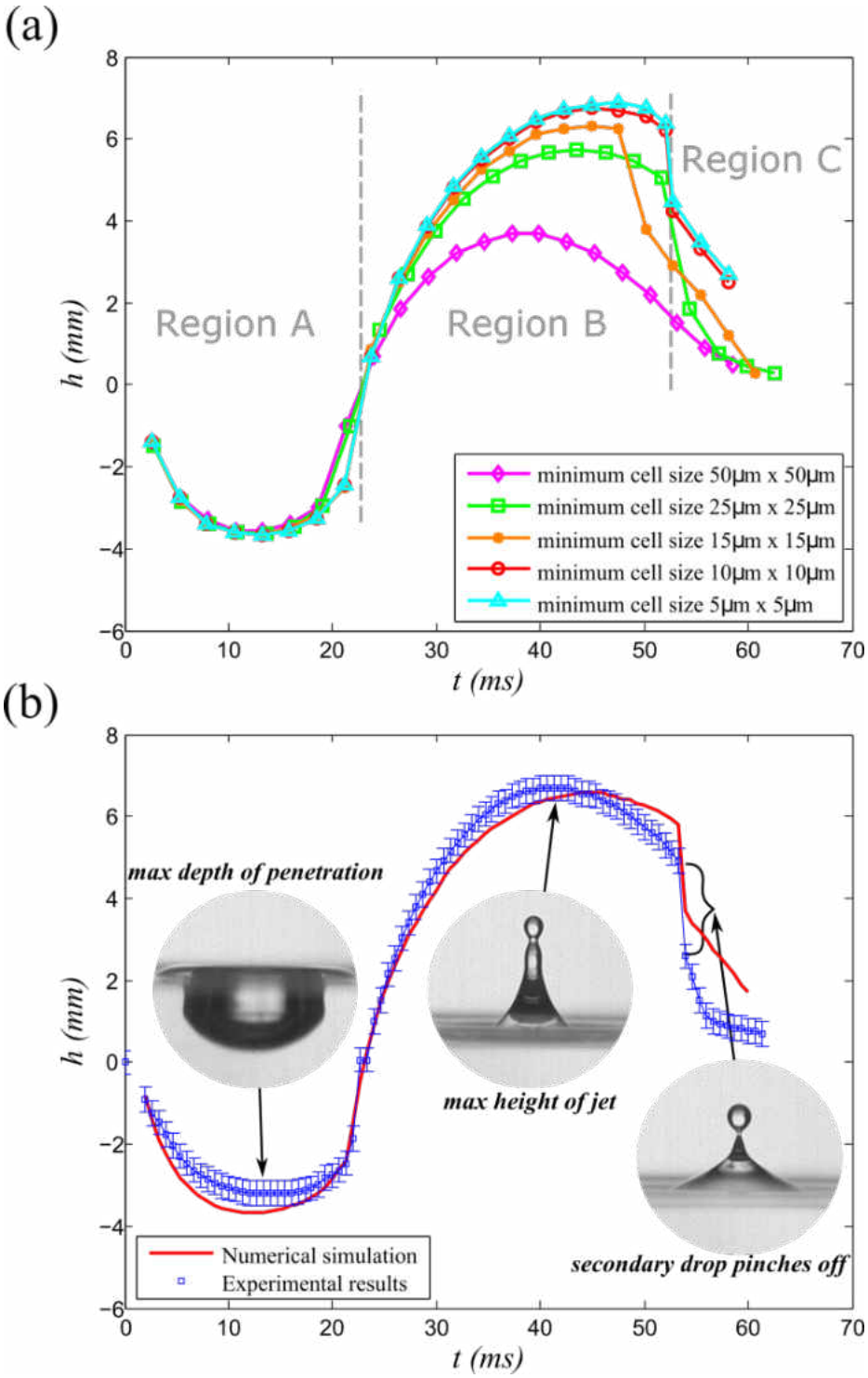

Figure 4-4: (a) Grid convergence based on the variation of the height of the cylindrical column for a silicone oil 5cSt droplet, 1.8 mm diameter, impact on liquid pool (Re = 324, We = 135, and Oh = 0.36). (b) Quantitative comparison of the numerical results with experiments.

The CFD model predicted the critical Weber number for combinations of liquid properties and droplet diameter that led to Ohnesorge numbers of 0.007, 0.014, 0.044, and 0.060. In order to find out the transition boundaries between the jet formation and its breakup with subsequent formation of secondary drops, different impact velocities were tested. Nearly 30 numerical simulations, supplemented by 50 experiments (run three times for each *We*-*Oh* combination for repeatability) were carried out. A high-performance computing cluster was used to run all simulations.

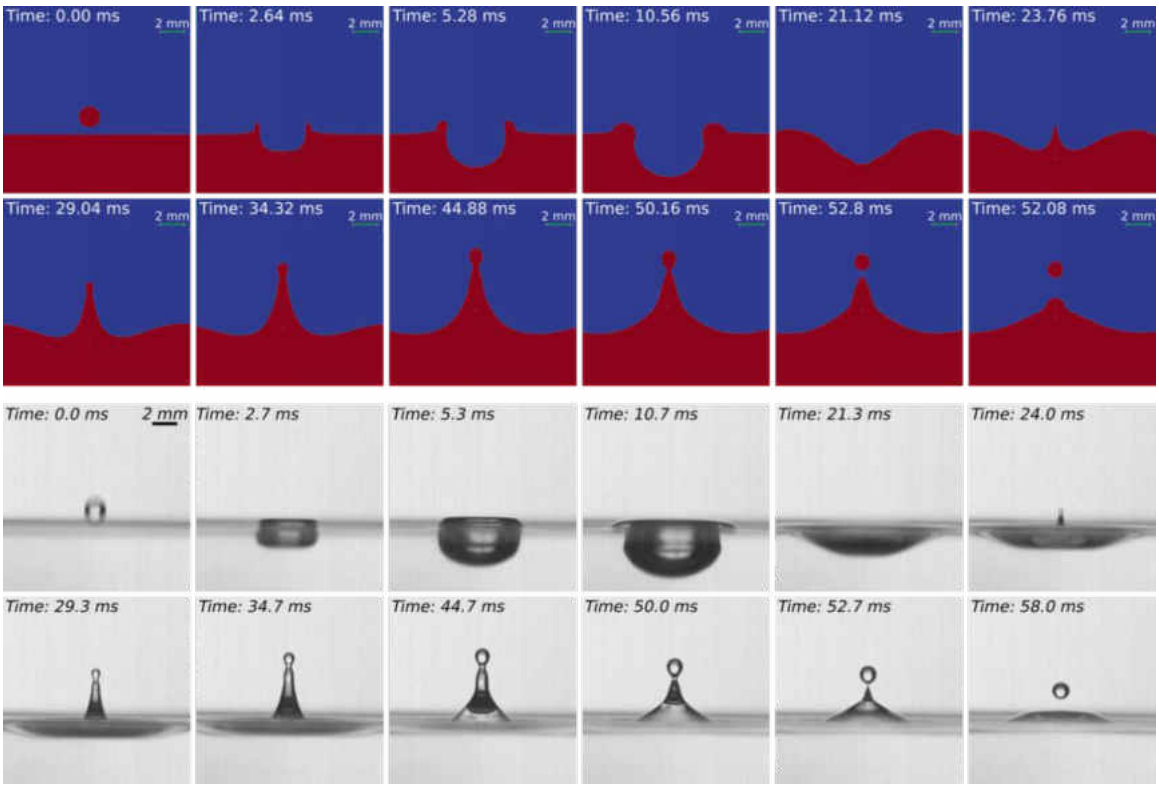

Figure 4-5: Quantitative comparison of the numerical and experimental results. Time evolution of the Rayleigh jet for the impact of a silicone 5 cSt droplet with its own pool (*Re* = 324, *We* = 135, *Oh* = 0.036).

CHAPTER 5: RESULTS AND DISCUSSION

The content of this chapter has been published in article: "E. Castillo-Orozco et al., Droplet impact on deep liquid pools: Rayleigh jet to formation of secondary droplets, Phys. Rev. E, 2015" [38].

5.1 Image processing results

The sequences of stages, registered by the high speed camera, involve the initial droplet impact, crater formation, central (Rayleigh) jet evolution, subsequent jet breakup, and pinch-off of the secondary drops. In order to analyze the images more efficiently, a MATLAB code was developed for image processing (included in Appendix A). This code converts the gray scale images into binary and allows for extraction of impact characteristics mentioned earlier. The proper calibration factor is employed to convert pixel to millimeter. Figure 5-1 shows four binary images from MATLAB, which are used to track the variation of the central column in time. These images correspond to silicone oil 5 cSt, D_o = 1.8 mm, and U = 1.8 m/s (Table 5-1).

Table 5-1: Information extracted from experiments using in-house developed MATLAB code for the same case shown in Fig. 5-1. (t = 0 is when the droplet contacts the pool surface).

Event	**Details**
Droplet impact velocity	1.8 m/s
Evolution of crater depth	14 ms, from formation up to maximum depth
Critical height of Rayleigh jet	6.69 mm after t = 42 ms
Size of secondary droplet	1.45 mm diameter (pinch-off occurs at t = 54 ms)

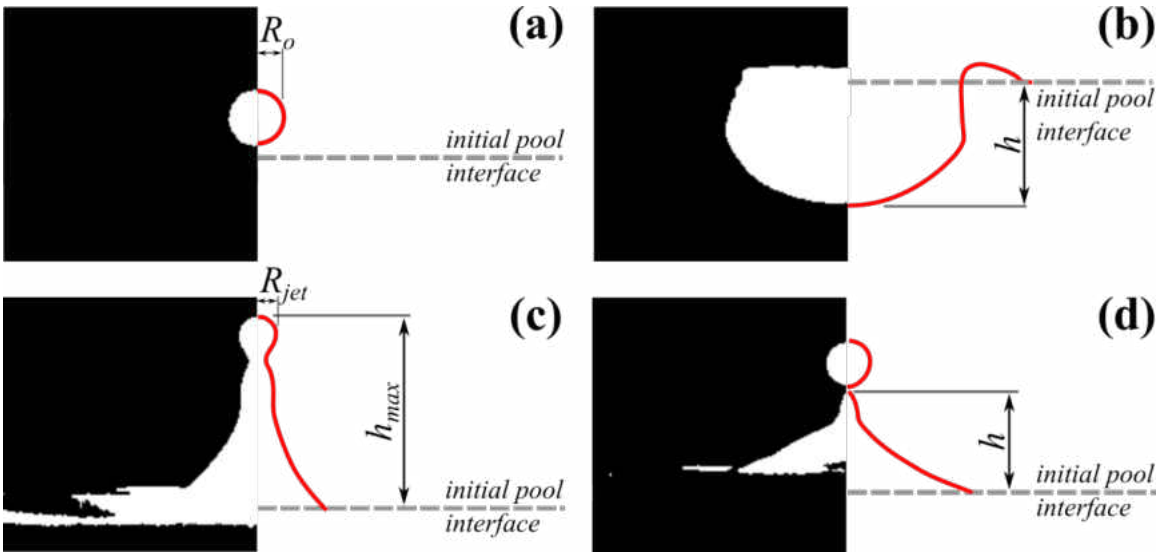

Figure 5-1: Binary images used for image processing. Sequence of stages of a silicone oil 5 cSt droplet (*We* = 135, *Oh* = 0.036). (a) Droplet 0.5 ms before impact upon liquid pool, (b) maximum depth of crater, (c) maximum height of Rayleigh jet, and (d) pinch-off of the secondary droplet.

5.2 Physics behind Rayleigh jet formation and breakup

When a droplet impacts the pool with high kinetic energy, the impact causes large disturbances to the pool which forms a deep crater followed by a Rayleigh jet. The Rayleigh jet has the potential to breakup due to Rayleigh-Plateau instability, as shown in Fig. 5-2. The Rayleigh-Plateau instability occurs when surface waves begin to form under the influence of surface tension. When the surface waves are of varicose mode and are long waves, a pinched region forms on the jet as shown in Fig. 5-2 b. As the amplitude of the long wave ($\lambda=2\pi R_{jet}$) begins to grow, pressure begins to build up within the pinched region as shown in Fig. 5-2c. The jet breaks up once the growth rate peaks. It should be noted that the wavelength is approximately the circumference of the jet and the growth rate for a jet has a capillary time scale, $t_{cap} \sim (\rho R_{jet}^3/\sigma)^{1/2}$, where R_{jet} is the radius of the jet

[39]. The current experiments suggested that R_{jet} is of the same order of magnitude as the initial radius of the droplet (R_o), therefore $t_{cap} \sim (\rho R_o^3/\sigma)^{1/2}$. The viscosity of the jet plays no significant role on the range of unstable wavelengths. However, at higher *Oh*, viscosity can slow down the growth rate of the unstable waves with a viscous time scale of $t_{visc} \sim \mu R_{jet}/\sigma$ [40]. Additionally, the ratio of t_{visc} to t_{cap} represents the Ohnesorge number. Therefore, *Oh* is an indicator of how much the breakup time has lagged. As is seen in Table 5-2, that capillary time scale and breakup time are of the same order, even though the former is approximately 3 to 10 times smaller than the latter. Thus, the capillary time scale is the appropriate scale to normalize breakup time. The breakup time is calculated from the time at which the jet emerges from the interface until it reaches the maximum height where it pinches off (Fig. 5-3). The non-dimensional time, $t^*_{breakup}$, is seen to increase linearly with *Oh* up to *Oh* = 0.06, beyond which the curve becomes non-linear.

Table 5-2: Time scales of the problem sorted based on the Ohnesorge number (fluids).

Liquids	***Oh***	$t_{breakup}$ ***(ms)***	t_{cap} ***(ms)***	t_{visc} ***(ms)***
Water	0.0033	22.7	5.21	0.02
Potassium hydroxide	0.0033	18.0	5.94	0.02
Silicone oil 1 cSt	0.0070	24.7	5.81	0.04
Ethanol	0.0085	28.7	5.68	0.05
Silicone oil 2 cSt	0.0140	27.0	5.81	0.08
Silicone oil 5 cSt	0.0360	30.0	5.81	0.21
Silicone oil 5 cSt	0.0440	28.0	3.99	0.18
Silicone oil 8 cSt	0.0600	35.0	5.80	0.35
Silicone oil 10 cSt	0.0716	36.0	5.81	0.42
Ethylene glycol	0.0815	38.7	5.54	0.45
Silicone oil 13 cSt	0.0907	65.5	6.32	0.57

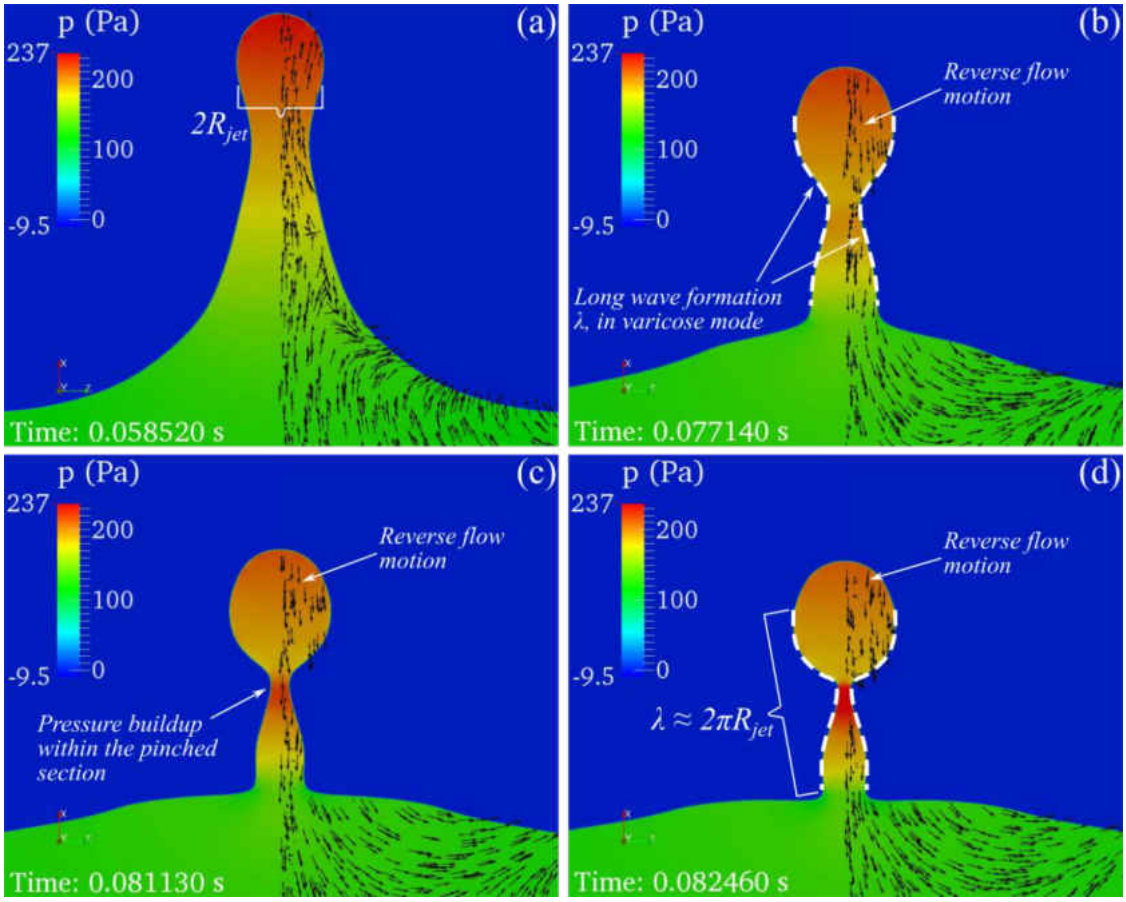

Figure 5-2: Pressure buildup in the pinched region after the impact of a silicone oil 1.8 mm droplet (10 cSt) with impact velocity of 2.5 m/s (*We* = 261, *Oh* = 0.0716). Pressure field is shown on each image and velocity vectors of the central Rayleigh jet are shown on right side of each image. Some vectors have been removed for clarity.

Along with viscosity, the fluid motion of the jet can lag the breakup time as well. Since the emerging jet opposes gravity, the velocity of the jet reverses such that the fluid motion is directed towards the pool, as shown in Fig. 5-2. This reverse motion causes fluid to displace into the pinched section. While the velocity of the reverse fluid motion is not high enough to stabilize the jet, the reverse motion lags the breakup time. If the pinched section recedes back into the pool in a shorter time than the breakup time, breakup will not occur. Therefore there is a critical height that the jet must reach for

breakup to occur. These critical heights are visualized in Fig. 5-4 and later quantified non-dimensionally in Fig. 5-5 and Fig. 5-6.

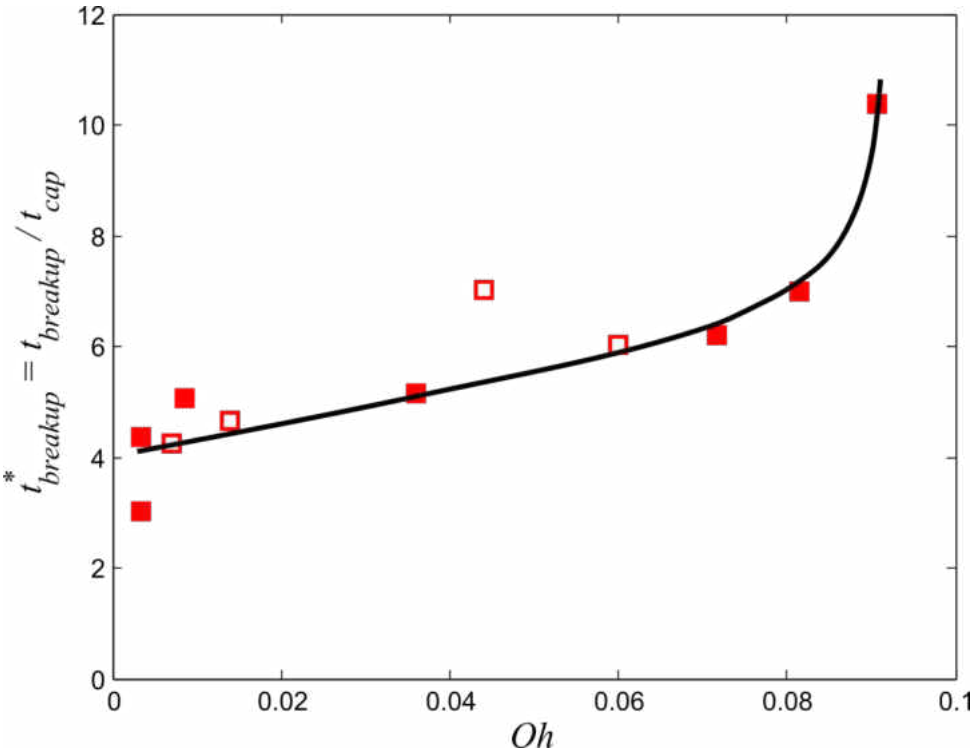

Figure 5-3: Normalized breakup time of the Rayleigh jet vs. Ohnesorge number. The filled and unfilled symbols represent the experimental and numerical data respectively.

In addition to the above phenomenon, it is observed that the reverse motion also occurs inside the droplet and the droplet has no distortion as the pinched section recedes back into the deep pool. The wavelength of the long wave does not significantly change while the amplitude grows. Therefore, the breakup of the pinched region is due to the Raleigh-Plateau instability caused by the temporal growth rate of the long wave. For partial coalescence to have occurred, the capillary waves would have traveled up the droplet causing the droplet to be distorted and pulled upward which leads to a pinch-off by stretching separation [14, 15].

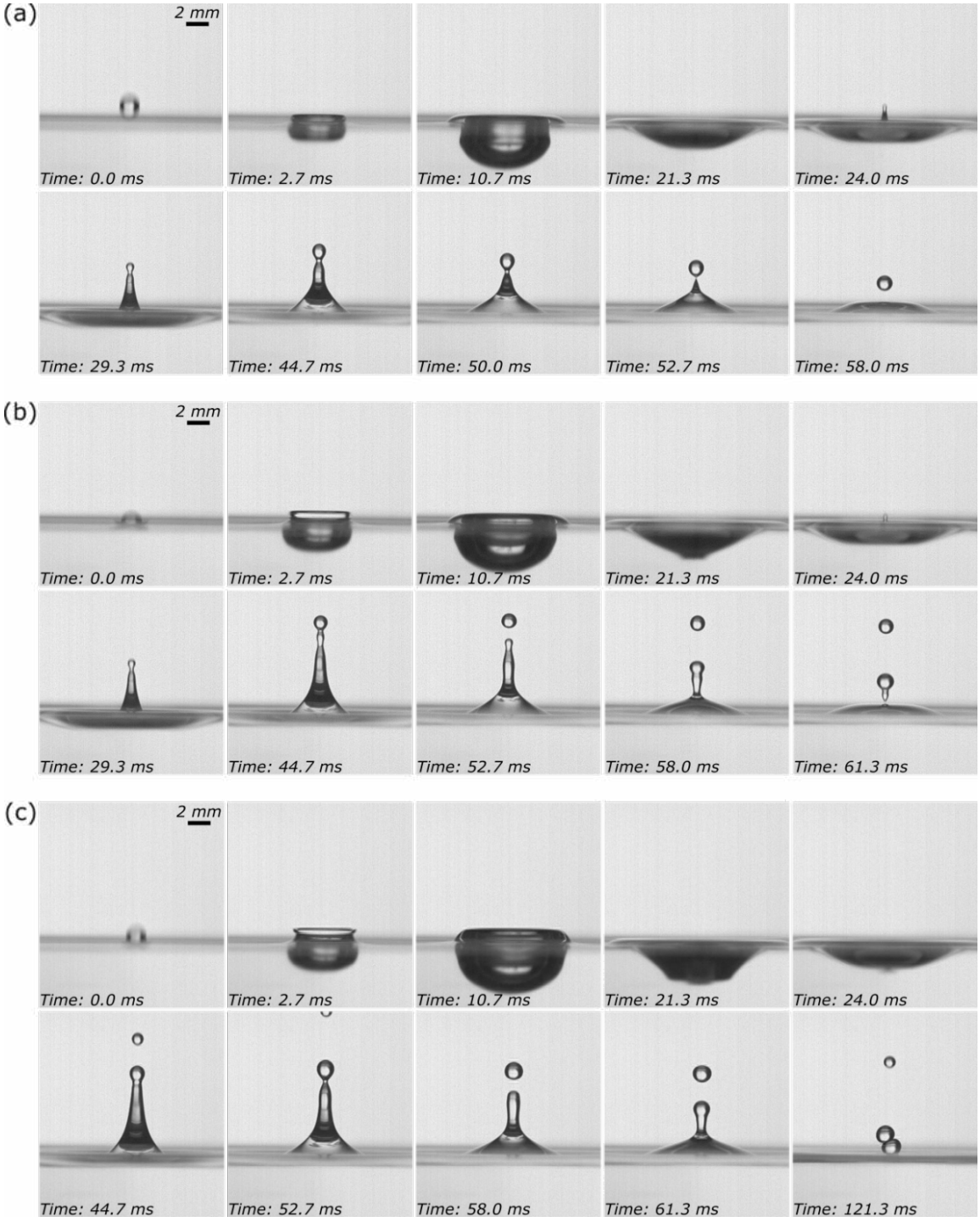

Figure 5-4: Visualization of droplet impact process for a 5 cSt silicone oil drop at selected times for (a) U = 1.8 m/s (We = 135), (b) U = 2.1 m/s (We = 184), and (c) U = 2.3 m/s (We = 221). All cases correspond to Oh = 0.036.

Typically, increase in impact velocity causes larger depth of crater and height of jet. It is also reasonable to conclude that the probability of jet breakup increases with impact velocity. Viscosity of fluids tends to damp down the effect of the impact. For silicone oil 5 cSt, if U = 1.8 m/s (We = 135, Oh = 0.036), only one secondary drop is formed. At 2.1 m/s (We = 184), two secondary drops are formed, and at 2.3 m/s (We = 221) three secondary drops are formed (Fig. 5-4). Interestingly for silicone oil 20 cSt, even at velocities three times greater than critical impact velocity of silicone 5 cSt, no pinch-off was observed.

In the particular case shown in Fig. 5-4, where different numbers of secondary drops are formed, the secondary droplets display sizes (diameters) of $0.58D_o$ to $0.94D_o$. It was observed that the size of secondary droplets varies for the different fluids and impact velocities that were tested in this study, but the order of magnitude for these drops remains the same as the mother droplet.

Among the cases that result in Rayleigh jet breakup and subsequent secondary droplet formation, the height of the Rayleigh jet was tracked up to the point where the first secondary droplet pinches off. Figure 5-5 depicts the variation of the normalized maximum height of Rayleigh jet as a function of impact We.

The higher the Ohnesorge number is, the lower the height of the Rayleigh jet. When Oh number increases, viscous forces become dominant over surface tension forces, which hinder the development of the jet as the capillary waves are not able to vertically stretch the droplet. The normalized height is also compared with its respective normalized time in Fig. 5-6a, and 5-6b. Properties of the liquid pool have an important role here. Higher Oh number tends to retard the evolution of the jet and subsequently the

pinch-off process, in other words it takes longer time for the jet to reach a specific height compared to low *Oh* number fluids. It is noticeable that for silicone oil 13 cSt, which has the critical Ohnesorge number, the variation of maximum height of the jet with time is no longer linear. Moreover, Figure 5-6b shows that there is a direct relationship between the non-dimensional maximum height of the Rayleigh jet to form its first secondary droplet and the time associated with it. This relation is presented in Eq. (18), where t^*_{hmax} is the normalized time required for the jet to reach its maximum height, and h^*_{max} is the normalized maximum height of Rayleigh jet.

$$h^*_{max} = 0.91 t^*_{hmax} \quad (18)$$

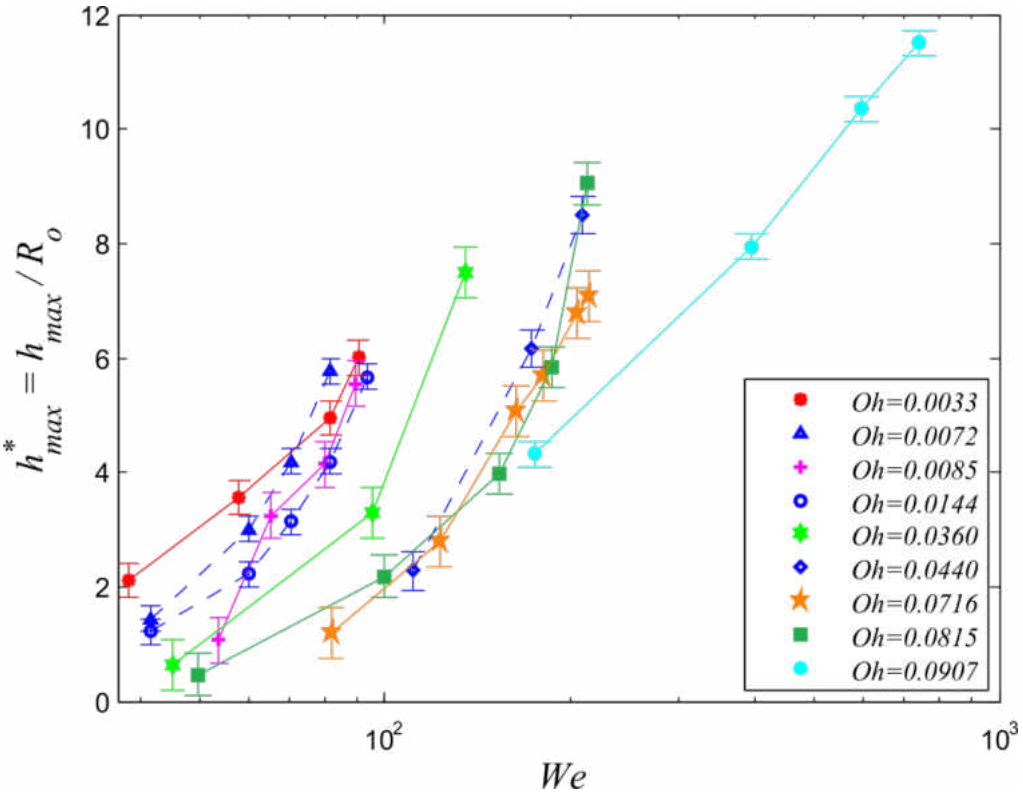

Figure 5-5: Normalized maximum height of the Rayleigh Jet, h^*_{max} up to the pinch-off of the first secondary drop vs. impact Weber number, *We*.

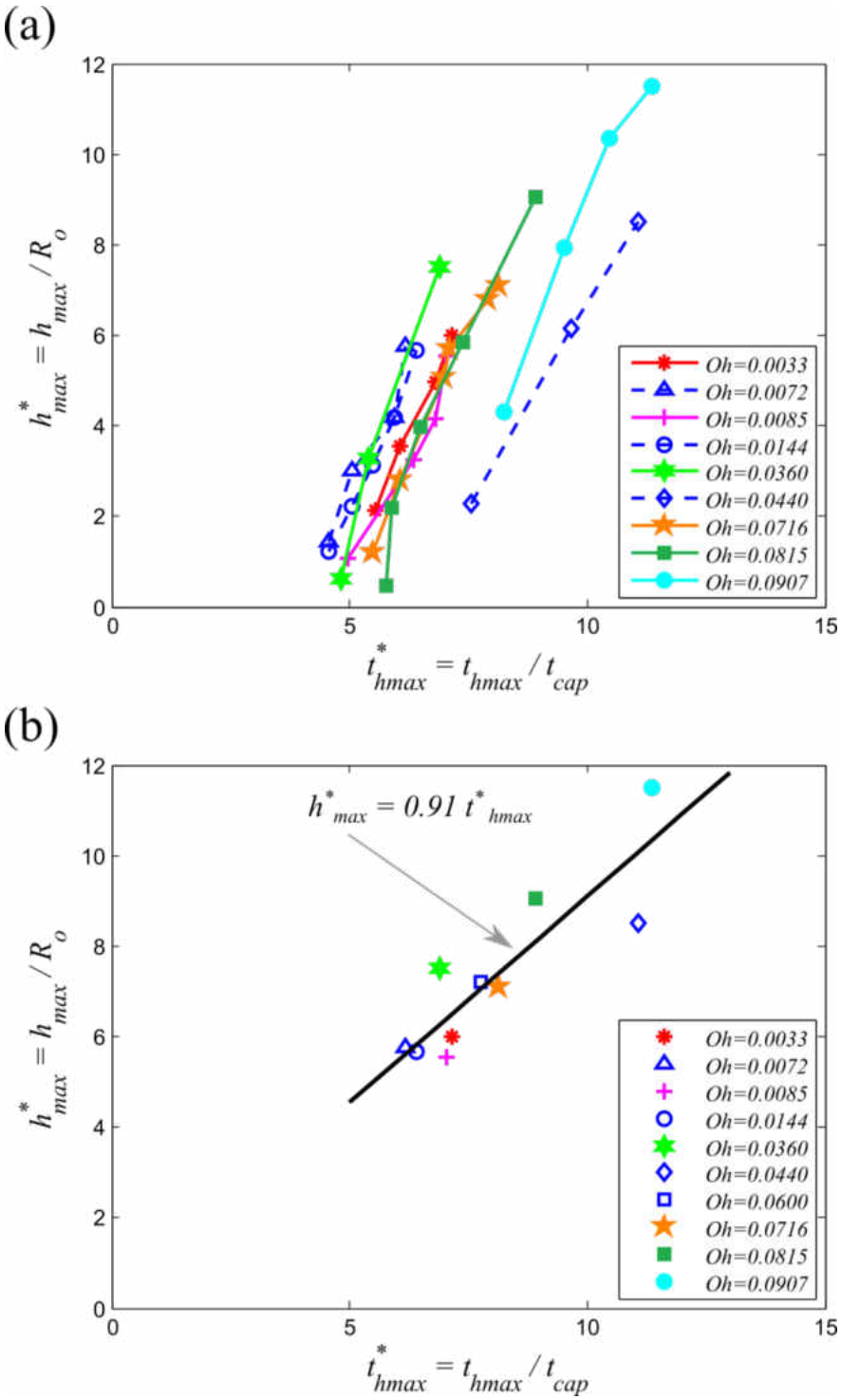

Figure 5-6: (a) Normalized maximum height of the Rayleigh jet up to the pinch-off of the first secondary drop vs. normalized Time, (b) Maximum height of Rayleigh jet for critical cases (at which pinch-off of the first secondary drop occurs) normalized by initial drop radius vs. normalized time

Figure 5-7 demonstrates the evolution of cavity and the subsequent central jet for cases that show the Rayleigh jet breakup. The time is normalized with capillary time while the height of the jet and depth of penetration are normalized with droplet size. From Fig. 5-7a it can be seen that the depth of cavity at the time of jet eruption and pinch-off of first secondary drop decreases with *Oh*. In general, the fluids of lower viscosity show deeper crater. This behavior was also observed by Ghabache et al. [22] in the jet formation from bursting of bubble. The evolution of the height of the central jet up to the pinch-off of first secondary drop is shown in Fig 5-7b. Indeed, *Oh* number plays an important role in retarding the pinch-off process. By relating the dynamics of the cavity (Fig. 5-7a) to the height of the jet (Fig. 5-7b), it can be concluded that for higher *Oh* numbers (for fluids of higher viscosity), the effective size of the cavity is smaller. On the other hand, the critical height of the jet to pinch-off for fluids of higher viscosity is larger.

Figure 5-8 compares the shape of crater for ethanol, silicone oil 5 cSt, and 10 cSt. As observed by Ghabache et al. [22], it can also be noticed here that as viscosity increases, the edges of the crater become smoother, particularly for silicone oil 10cSt (Fig. 5-8c). Figure 5-8d compares the overlap of collapsed cavity for the aforementioned fluids.

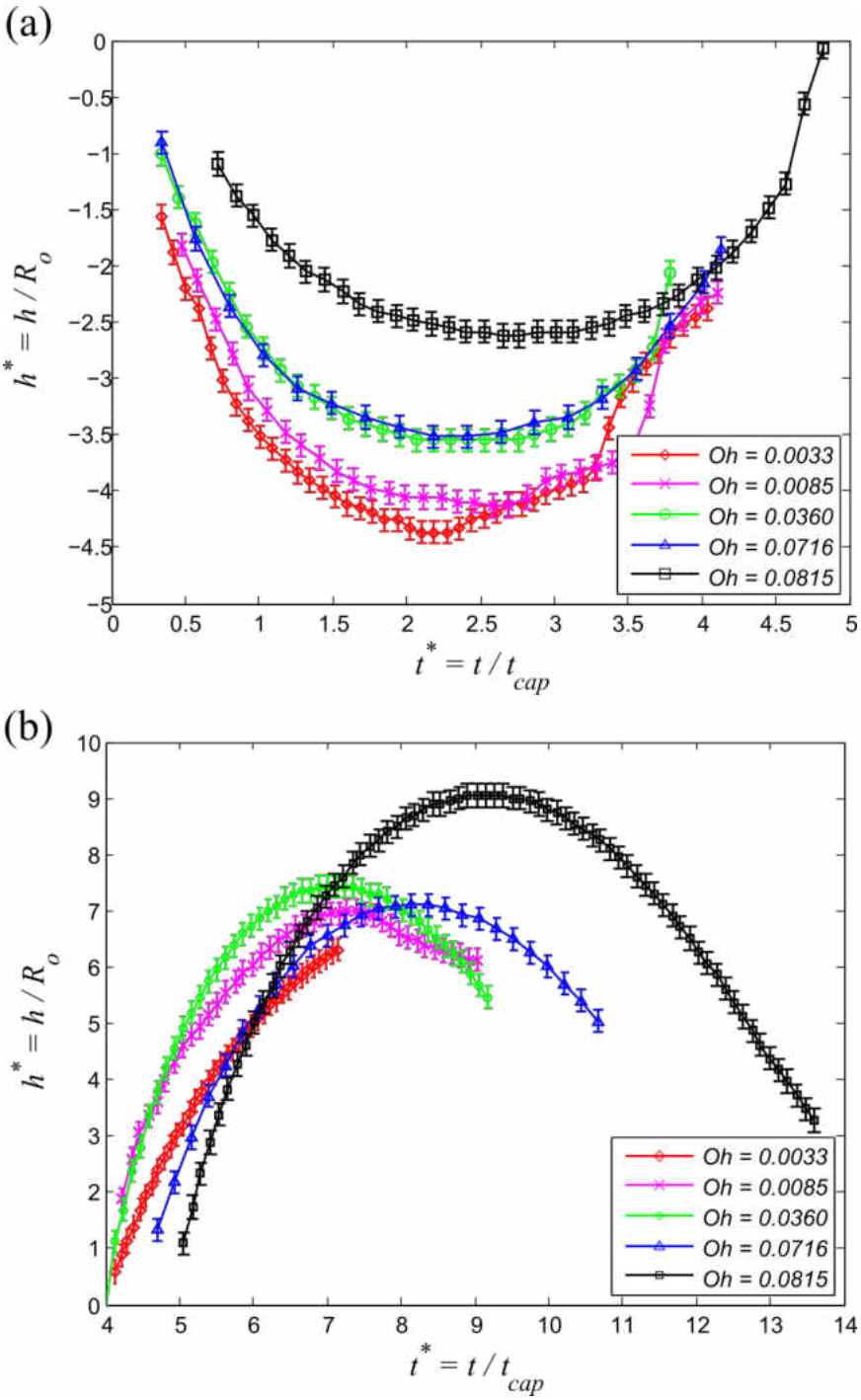

Figure 5-7: Tracking interface of (a) cavity and (b) central jet. The horizontal axis is normalized by capillary time and the vertical axis by initial droplet radius.

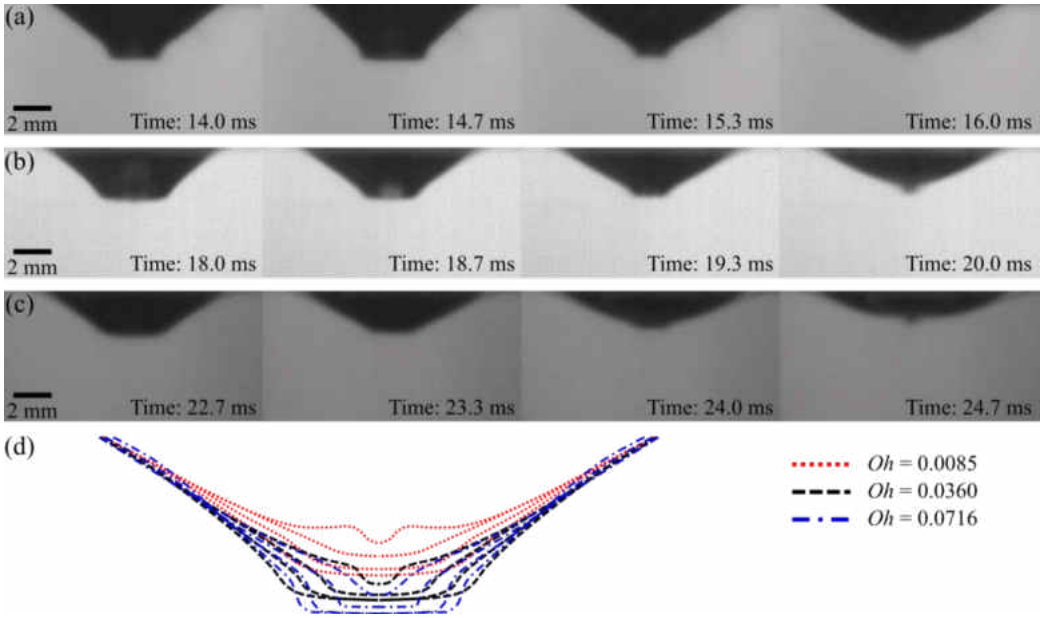

Figure 5-8: Dynamics of cavity for three fluids at selected times. (a-c) depth of crater for ethanol, silicone oil 5 cSt, and silicone oil 10 cSt, (d) overlap of collapsed cavity for these fluids.

5.3 Effects of impact velocity, surface tension and viscosity

The experiments were performed using distilled water, potassium hydroxide (KOH), ethanol, ethylene glycol, silicone oils 5, 10, 13, 14, 16, 18 and 20 cSt, as summarized in Table 3-1. The silicone oils have similar surface tension (~ 20 mN/m) and densities (~ 940 kg/m3), but different viscosities. Except for water, the results were highly repeatable for the abovementioned fluids. Water did not display consistent results under the same conditions, perhaps due to its impurities, an observation that was also made by others [41]. In order to confirm the water results, potassium hydroxide was tested since it has similar properties leading to the same Ohnesorge number as water (Table 3-1). Among these fluids, the silicone oils showed the best repeatability at all stages, from the height of Rayleigh jet to the number of secondary droplets at a certain impact Weber number.

The impact velocities were measured using image processing techniques and compared with $U = (2gH)^{1/2}$ from conversion of potential energy into kinetic energy, where H is the release height. It is important to note that the values of U from experiments were always lower than that of theory, especially if the height exceeded 1 m. This is due to the drag force acting on the droplet. Therefore for consistency, the experimentally obtained impact velocities were used to calculate the non-dimensional parameters shown in this study.

When a droplet impacts the pool of the same fluid, it penetrates through the interface and forms a crater. If the impact velocity is high enough, a central Rayleigh jet will form. Under certain conditions, the tip of the jet pinches off due to Rayleigh-Plateau instability and the secondary droplet forms. Many parameters can affect this behavior of which viscosity, surface tension and impact velocity are the most important. The parameter of particular significance to identify the boundaries of transitions between no breakup and Rayleigh jet and later into crown splash is the Weber number. The impact Weber, *We*, at which the jet breaks up and the secondary droplet forms is called the critical Weber number. When viscous effects are under consideration to study instability, *Oh* is a more appropriate parameter as it isolates the property effects more. *Re* has also been used to classify the morphologies of crown droplets on a *We*-*Re* map [8]. In Fig. 5-9a and 5-9b, regime maps for Rayleigh jet breakup, crown splash and subsequent formation of secondary droplets are plotted both as *We* vs *Re* and We vs *Oh* respectively. Each Ohnesorge number represents a distinct fluid, whereas the variation in Weber number is due to changes in release height of the droplet.

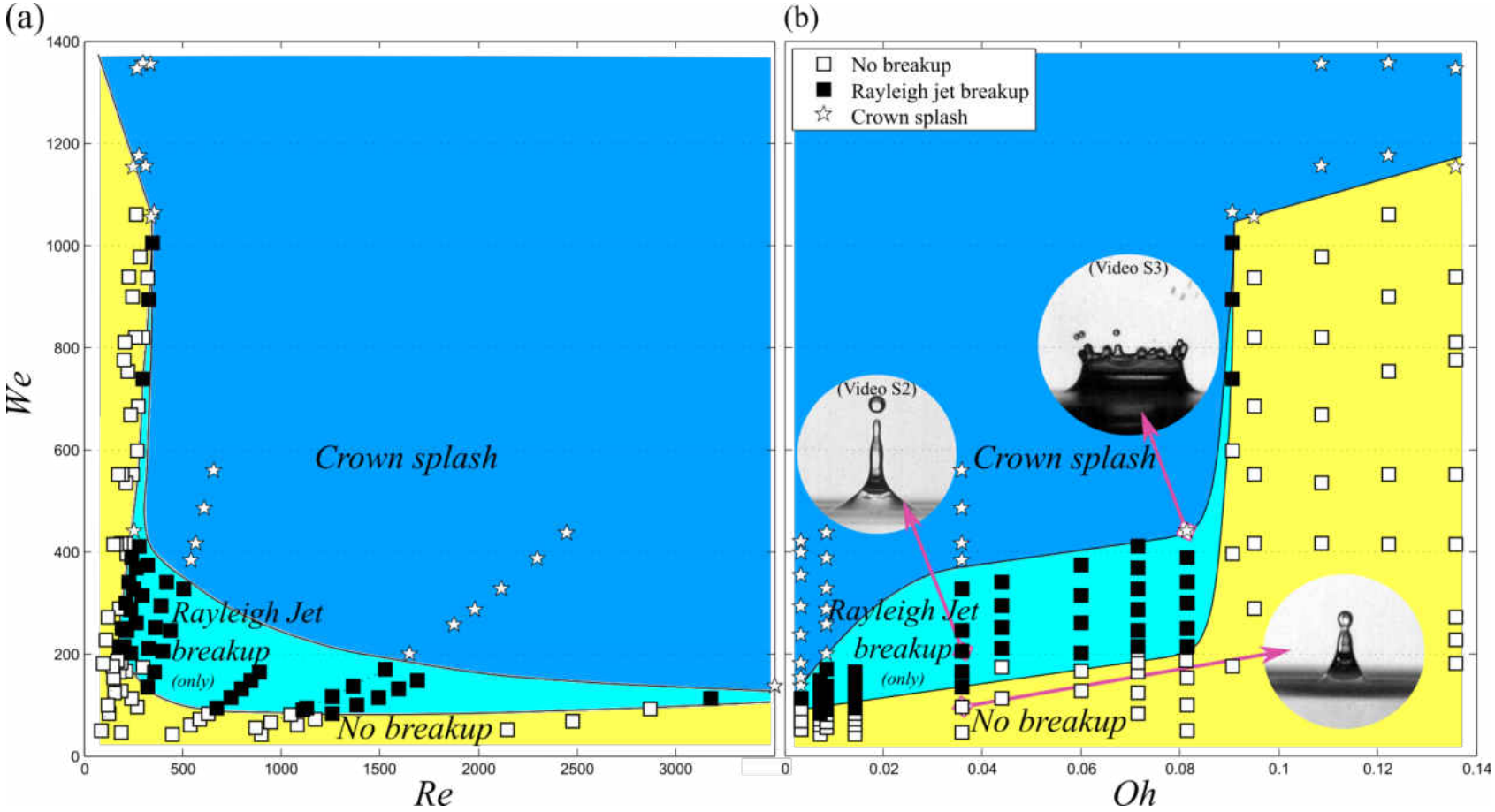

Figure 5-9: (a) and (b) Regime maps for Rayleigh jet breakup and subsequent secondary droplets formation based on *Re* and *Oh* respectively. Filled markers represent the cases where breakup took place and single or multiple secondary droplets were observed. Blank and star symbols represent no breakup and crown splash respectively. Ohnesorge number of 0.007, 0.014, 0.044, and 0.060 were obtained from numerical simulations. The rest of the cases were obtained from experimental results. Videos S2 and S3 can be found as supplementary material representing each of these flow regimes both experimentally and numerically.

For a combination of $Oh \leq 0.091$ and Weber numbers beyond the critical value, the jet breakup leads to one or multiple secondary droplets that are on the order of $0.5D_o$ to $2D_o$. At low impact *We* number, the kinetic energy cannot overcome the surface tension forces. Depending on the impact velocity, in some cases, both Rayleigh jet breakup and crown splash can occur (e.g. $Oh = 0.0815$ and $We = 440$).

As viscosity increases, the kinetic energy at impact dissipates quicker, causing smaller disturbance to the pool, which decreases the height of the jet. In addition, the growth rate of Rayleigh-Plateau instability becomes smaller as viscosity increases [42]. Smaller growth rate further lags the breakup time. Therefore, for breakup to occur, the impact velocity or Weber number must increase as *Oh* number increases. However, if the Weber number increases high enough, the surface waves on the Rayleigh jet become short wave dominant. Short waves tend to stabilize the pressure fluctuations in the jet such that breakup does not occur [43] Therefore; there is a cutoff *Oh* at which Rayleigh-Plateau instability will no longer occur. From Fig. 5-9, it is observed that the cutoff *Oh* is ≈ 0.091. Existence of a critical Ohnesorge number is also confirmed by Blanchette and Bigioni [15], even though the size and impact velocity of droplets were not comparable with this study.

Interestingly, crown splash is observed to occur regardless of the cutoff *Oh*. Upon coalescence, the kinetic energy of the droplet is partially dissipated due to the viscous forces, the rest being transformed into surface energy distributed over a large surface area. At high impact velocities, the remainder of the kinetic energy results in the detachment of the lamellas from the liquid periphery. Typically, lower surface tension

and viscosity combined with high impact velocity facilitate the crown formation. Viscosity is important since it determines the splash morphology. For high viscosity fluids, the secondary drops detach only after the complete development of crown but not in the early stages. However, for fluids with relative low viscosity the crown splash can take place at early stages. The sequence of crown formation is presented in Fig. 5-10.

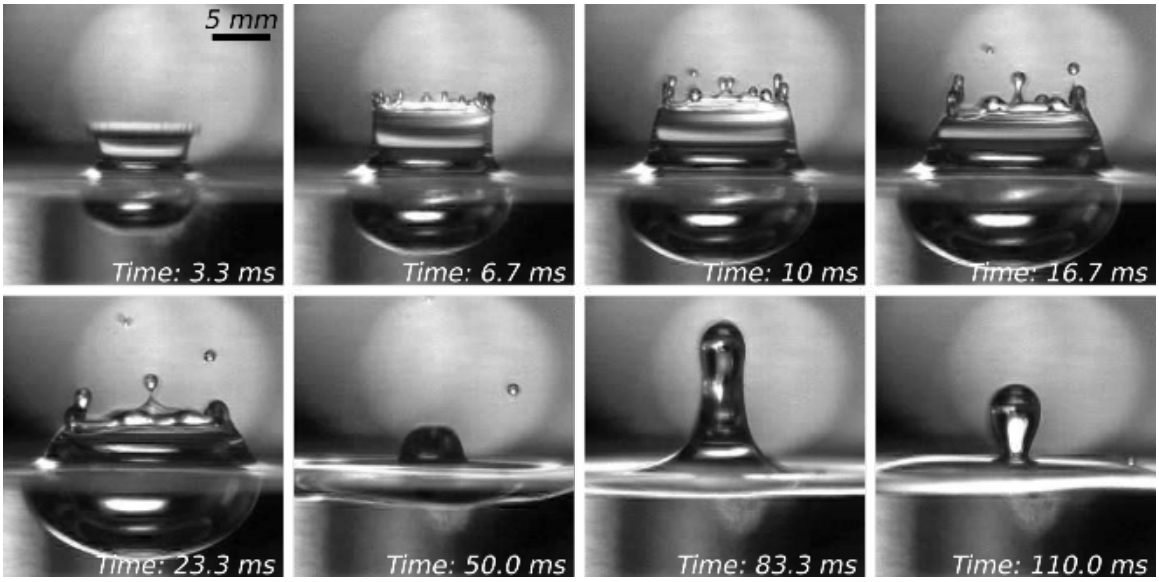

Figure 5-10: Visualization of crown splash and Rayleigh jet formation for a silicone oil 20 cSt droplet impingement upon pool of same liquid. *Re* = 250, *We* = 1153, *Oh* = 0.1358. Time after initial droplet impact (D_o = 2.0 mm, U = 5.01 m/s) is shown in each snapshot.

CHAPTER 6: CONCLUSIONS

In summary, the influence of fluid properties and impact velocity upon Rayleigh jet and pinch-off of secondary droplets have been studied within the impact of a liquid droplet on a pool of identical fluid. To better understand the physical phenomena and confirm our observations, numerical simulations based on VOF and CSF methods were deployed. Increase in impact velocity (Weber number) increases the height of the thin column of fluid that emerges from the liquid pool. Under certain fluid conditions, the dissipation of this extra kinetic energy along with the surface tension forces produces instabilities in the neck of the jet. This could result in jet breakup and formation of secondary droplets. However, if the fluid has a high viscosity (i.e. high Ohnesorge number), a large portion of kinetic energy is dissipated thus Rayleigh jet breakup may never occur. In other words, both the formation of the jet and its further breakup require a balance between viscous, capillary and surface tension forces. A *We-Oh* plot shows three regimes for $0.0033 \leq Oh \leq 0.136$. For Weber numbers beyond the critical value and $Oh \leq 0.091$ the jet breakup occurs (Rayleigh jet breakup regime). While for $Oh > 0.091$, the jet breakup is suppressed regardless of the Weber number. In addition, high impact velocity initiates the crown formation and if further intensified it can disintegrate it into numerous secondary droplets. Since more viscous fluids tend to dampen the impact, they mitigate the occurrence of crown splash except at higher impact velocities. In addition, a correlation is proposed for normalized time with respect to the normalized maximum height of jet.

APENDIX A: MATLAB CODE FOR IMAGE PROCESSING

```
%%%%%%%%%%%%% ROUTINE FOR IMAGE PROCESSING OF PHOTOGRAPHS %%%%%%%%%%%%%

   clc;
   clear all;
   close all;


%% DATA AND IMPUT

   nOD = 0.82  % needle OD (mm)
   fps = 2000  % frames per second (1/s)
   % Specify x-poitions where you want to track the interface
     xTrack1 = 369         % Outside of pool
     xTrack2 = 400         % Inside of pool
   % Specify y-interface
     yInter = 244
   % To limit the usage of factor 1 & 2
   firstPic = 10         % first picture to analyze (it must be 2
pictures before impact)
   impactPic = 12        % picture that corresponds to impact (initial
time)
   firstTrackPic = 15    % track the interface from this picture
   limitPic = 85         % first picture, where the factor 1 must be
used
   numZeros = firstTrackPic-impactPic;
   numUsedForImpact = impactPic-firstPic;
   numFactorLim = limitPic-firstPic;   % factor limit
   numFactorLimCor = numFactorLim-numUsedForImpact;



%% GET CONVERSION FACTOR mm/px

   nRef = imread('needleRef.jpg');
   bI = imread('needleBackGround.jpg');
   nRefSub = imsubtract(bI,nRef);
   nGray = rgb2gray(nRefSub);
   nGrayAdj = imadjust(nGray);
   n = im2bw(nGrayAdj);
   n = bwareaopen(n,1000); % Area segmentation (A<1000)
   [nr,nc] = size(n);
   y1 = round(0.45*nr)
   y2 = round(0.8*nr)
   x1 = round(nc/3);       % region 1. Outside of pool
   x2 = round(nc*2/3);     % region 2. Inside of pool
   zeros1 = find(n(y1,x1:x2)==1);
   zeros2 = find(n(y2,x1:x2)==1);
   nDiaPx1 = zeros1(end)-zeros1(1);
   nDiaPx2 = zeros2(end)-zeros2(1);
   factor1 = nOD/nDiaPx1   % factor mm/px for surface outside liquid
pool
   factor2 = nOD/nDiaPx2   % factor mm/px for surface inside liquid
pool
   % Plot figure 1
```

```
     g1 = figure (1);

subplot(2,2,1),imshow(nRefSub);subplot(2,2,2),imshow(nGrayAdj);subplot(
2,2,3),imshow(n);
     title('Get factor mm/px');



%% DROP DIAMETER AND IMPACT VELOCITY

   bI = imread('backGroundRef.jpg');
   pdir = dir('*m*.jpg');

   for jj=1:2
       pfullname = pdir(jj).name;
       imagename = pfullname;
       I = imread(imagename);             % Read image
       Z = imsubtract(bI,I);              % Subtract back ground from
image
       picGray = rgb2gray(Z);             % Get gray scale image
       picGrayAdj = imadjust(picGray);    % Adjust the gray scale image
       picBw = im2bw(picGrayAdj);         % Convert to binary image
       picBw = imclearborder(picBw);      % Clear borders
       picBw = bwareaopen(picBw,800);
       picBwFil = medfilt2(picBw, [3,3]);% Apply filter
       [nr,nc] = size(picBwFil);
       % Find ones of droplet
       dropLength = find(picBwFil(1:yInter,xTrack1)==1);
       % Get drop center
       dropCenter = round((dropLength(1)+dropLength(end))/2);
       % Find ones of drop diameter
       dropD = find(picBwFil(dropCenter,1:nc)==1);
       dropD = (dropD(end)-dropD(1));     % Get drop diameter in pxs
       dropDiam(jj) = dropD;              % Save drop diameter
       dropYpos(jj) = dropLength(1);      % Save drop position
  end
     dropDiam_mm =dropDiam*factor1                              % mm
     dropDiam_m = dropDiam_mm/1000
     dropVel = (dropYpos(1)-dropYpos(2))*factor1*0.001*fps  % m/s
  % Plot figure 2
    g2 = figure (2);

subplot(2,2,1),imshow(Z);subplot(2,2,2),imshow(picGrayAdj);subplot(2,2,
3),imshow(picBw);subplot(2,2,4),imshow(picBwFil);
    title('Drop impact diameter and velocity');



%% TRACK INTERFACE

   totalTime = 0:length(pdir)-1-numUsedForImpact;

   for ii=1:numZeros;
       filmPos(ii)=0;
```

```
   end

%% Track the interface inside of pool
   for jj=numZeros+1:numFactorLimCor;
       pfullname = pdir(jj+numUsedForImpact).name;
       imagename = pfullname;
       I = imread(imagename);
       Z = imsubtract(bI,I);
       picGray = rgb2gray(Z);
       picGrayAdj = imadjust(picGray);
       picBw = im2bw(picGrayAdj);
       %picBw = imclearborder(picBw);
       picBw = medfilt2(picBw, [5,5]);
       figure (jj)
       imshow(picBw)
       filmdepth = find(picBw(yInter:nr,xTrack2)==1);
       filmPos(jj) = -filmdepth(end)*factor2;
  end

%% Track interface outside of pool
   for kk = numFactorLimCor+1:length(pdir)-numUsedForImpact;
       pfullname = pdir(kk+numUsedForImpact).name;
       imagename = pfullname;
       I = imread(imagename);              % Read image
       Z = imsubtract(bI,I);               % subtract back ground from
image
       picGray = rgb2gray(Z);              % Get gray scale image
       picGrayAdj = imadjust(picGray);     % Adjust the gray scale image
       picBw = im2bw(picGrayAdj);          % Convert to binary image
       %picBw = imclearborder(picBw);      % Clear borders
       picBw = medfilt2(picBw, [3,3]);     % Apply filter
       %picBw = bwareaopen(picBw,5000);    % Area segmentation (A<5000)
       figure (kk)
       imshow(picBw)
       % Find ones from Central Jet
       filmheight = find(picBw(yInter:-1:1,xTrack1)==1);
       % Save Film position
       filmPos(kk) = filmheight(end)*factor1;
   end
       % Additional point for numZeros =2
         if numZeros == 2;
         filmPos(2)=filmPos(3)/2;
         end
   % Maximum jet height
     [maxHeight,i] = max(filmPos(:));
     maxHeight
     time_maxHeight = totalTime(i)/fps
     % Plot figure 3 (Interface evolution)
       totalTime_s = totalTime/fps;
       g3 = figure (3);
       plot(totalTime_s,filmPos,'-
or','LineWidth',1.0,'MarkerEdgeColor','r','Markersize',5);
       legend('Experiment');
       title('Interface-capturing at axisymmetric axis');
```

```
       xlabel([{'\itTime(s)'}],'FontSize',14,'FontName','Times New
Roman');
       ylabel([{'\itdh(mm)'}],'Fontsize',14,'FontName','Times New
Roman');



%% MEASURE DROP DIAMETER

   analyzeImage = 100; % Select image number to analize
   pfullname = pdir(analyzeImage+1-firstPic).name;
   imagename = pfullname;
   I = imread(imagename);
   Z = imsubtract(bI,I);
   Igray = rgb2gray(Z);
   IgrayAdj = imadjust(Igray);
   Ibw = im2bw(IgrayAdj);
   Ibw = imclearborder(Ibw);
   Ibw = medfilt2(Ibw, [3,3]);
   Ibw = imfill(Ibw,'holes');
   dropLoc = find(Ibw(:,xTrack1)==1);
   s = 1;
   i = 1;
   secondDropPx = 1;
   while s==1 & i<length(dropLoc);
         cond = dropLoc(i+1)-dropLoc(i);
         if cond==1;
            s = 1;
            secondDropPx = secondDropPx+1;
         else
               s = 0;
         end
         i = i+1;
   end
   secondDrop = secondDropPx*factor1
   % Plot figure 4
     figure (4);
     subplot(1,2,1),imshow(I);subplot(1,2,2),imshow(Ibw);



% Note:
% If get error: Attempted to access filmheight(0); index must be a
positive integer or logical. Error in ImageProcessing_picturesRev0
(line 133) filmPos(kk) = filmheight(end)*factor1;
% Solution: It will be needed to delete some pictures that give problem
or suppress "clear borders".
```

APENDIX B: BLOCK MESH AND BOUNDARY CONDITIONS - OPENFOAM

```
/*--------------------------*- C++ -*----------------------------*\
| =========                 |                                     |
|
| \\      /  F ield         | OpenFOAM: The Open Source CFD
Toolbox           |
|  \\    /   O peration     | Version:  2.3.1
|
|   \\  /    A nd           | Web:      www.OpenFOAM.org
|
|    \\/     M anipulation  |
|
\*---------------------------------------------------------------*/
FoamFile
{
    version     2.0;
    format      ascii;
    class       dictionary;
    object      blockMeshDict;
}
// * * * * * * * * * * * * * * * * * * * * * * * * * * * * * * * * * * * //

convertToMeters 1;
halfAngle 2.5;
radius 0.04;
radHalfAngle    #calc "degToRad($halfAngle)";
y               #calc "$radius*sin($radHalfAngle)";
minY            #calc "-1.0*$y";
z               #calc "$radius*cos($radHalfAngle)";
minZ            #calc "-1.0*$z";

vertices
(
    (0.0    0.0   0.0)    //0
    (0.04   0.0   0.0)
    (0.04   0.0   0.0)    //2
    (0.0    0.0   0.0)

    (0.0    $minY   $z)   //4
    (0.04   $minY   $z)
    (0.04   $y      $z)   //6
    (0.0    $y      $z)
);

blocks
(
    hex (0 1 2 3 4 5 6 7) (250 1 250) simpleGrading (1 1 1)
);

edges
(
```

```
    arc 4 7 (0.0   0  $radius)
    arc 5 6 (0.04  0  $radius)
);

boundary
(
    wallBottom
    {
        type wall;
        faces
        (
            (0 4 7 3)
        );
    }
    atmosphere
    {
        type patch;
        faces
        (
            (1 2 6 5)
        );
    }
    walls
    {
        type wall;
        faces
        (
            (4 5 6 7)
            (3 2 1 0)
        );
    }
    side1
    {
        type wedge;
        faces
        (
            (0 1 5 4)
        );
    }
    side2
    {
        type wedge;
        faces
        (
            (7 6 2 3)
        );
    }
);

// ************************************************************************* //
```

```
\*---------------------------------------------------------------------------*/
FoamFile
{
    version     2.0;
    format      ascii;
    class       volScalarField;
    location    "0";
    object      alpha1;
}
// * * * * * * * * * * * * * * * * * * * * * * * * * * * * * * * * * * * * //

dimensions      [0 0 0 0 0 0 0];

internalField   uniform 0;

boundaryField
{
    wallBottom
    {
        type            zeroGradient;
    }

    atmosphere
    {
        type             inletOutlet;
        inletValue       uniform 0;
        value            uniform 0;
    }

    walls
    {
        type            zeroGradient;
    }

    side1
    {
        type             wedge;
    }
    side2
    {
        type             wedge;
    }
}


// ************************************************************************* //
```

```
\*---------------------------------------------------------------*/
FoamFile
{
    version     2.0;
    format      ascii;
    class       volScalarField;
    object      p_rgh;
}
// * * * * * * * * * * * * * * * * * * * * * * * * * * * * * * * * * * * * //

dimensions      [1 -1 -2 0 0 0 0];

internalField   uniform 0;

boundaryField
{
    wallBottom
    {
        type            zeroGradient;
    }

    atmosphere
    {
        type            totalPressure;
        p0              uniform 0;
        U               U;
        phi             phi;
        rho             rho;
        psi             none;
        gamma           1;
        value           uniform 0;
    }

    walls
    {
        type            zeroGradient;
    }

    side1
    {
        type            wedge;
    }
    side2
    {
        type            wedge;
    }
}


// ************************************************************************* //
```

```
\*---------------------------------------------------------------------------*/
FoamFile
{
    version     2.0;
    format      ascii;
    class       volVectorField;
    location    "0";
    object      U;
}
// * * * * * * * * * * * * * * * * * * * * * * * * * * * * * * * * * * * * //

dimensions      [0 1 -1 0 0 0 0];

internalField   uniform (0 0 0);

boundaryField
{
    wallBottom
    {
        type            fixedValue;
        value           uniform (0 0 0);
    }

    atmosphere
    {
        type            pressureInletOutletVelocity;
        value           uniform (0 0 0);
    }

    walls
    {
        type            fixedValue;
        value           uniform (0 0 0);
    }

    side1
    {
        type            wedge;
    }
    side2
    {
        type            wedge;
    }
}


// ************************************************************************* //
```

LIST OF REFERENCES

[1] O. Reynolds, On the action of rain to calm the sea, Nature 11, 279-280 (1875).

[2] A.M. Worthington, A Study of Splashes, Longmans, Green, London, 129 (1908).

[3] M. Rein, Phenomena of liquid-drop impact on solid and liquid surfaces, Fluid Dyn. Res. 12, 61 (1993).

[4] R. Rioboo, C. Tropea, M. Marengo, Outcomes from a drop impact on solid surfaces, Atomization Sprays 11, pp. 155-165, (2001).

[5] C. Clanet, C. Béguin, D. Richard, and D. Quéré, Maximal deformation of an impacting drop, J. Fluid Mech. 517, pp. 199-208, (2004).

[6] S.L. Manzello, J.C. Yang, An experimental study of a water droplet impinging on a liquid surface, Exp. Fluids 32, 580 (2002).

[7] K.L. Pan and C.K. Law, Dynamics of droplet-film collision, J. Fluid Mech. 587, pp. 1-22 (2007).

[8] L.V. Zhang, P. Burnet, J. Eggers, R.D. Deegan, Wavelength selection in the crown splash, Phys. Fluids 22, 122105 (2010).

[9] D. Banks, C. Ajawara, R. Sanchez, H. Surti, and G. Aguilar, Effects of Drop and Film Viscosity on Drop Impacts onto Thin Films, Atomization Sprays, 23: 555-570 (2013).

[10] T. Tran, H. de Maleprade, C. Sun, D. Lohse, Air entrainment during impact of droplets on liquid surfaces, J. Fluid Mech. 726, R3 (2013).

[11] G. Agbaglah, M.-J. Thoraval, S.T. Thoroddsen, L. V. Zhang, K. Fezzaa, and R.D. Deegan, Drop impact into a deep pool: vortex shedding and jet formation , J. Fluid Mech. 764, R1 (2015).

[12] A. Prosperetti and H. Oğuz, The Impact of Drops on Liquid Surfaces and the Underwater Noise of Rain, Annu. Rev. Fluid Mech. 25: 577-602 (1993).

[13] Z. Mohamed-Kassim and E.K. Longmire, Drop Coalescence through a Liquid/Liquid Interface, Phys. Fluids 16, 2170 (2004).

[14] X. Chen, S. Mandre, and J.J. Feng, Partial coalescence between a drop and a liquid-liquid interface, Phys. Fluids 18 (2006) 051705.

[15] F. Blanchette and T.P. Bigioni, Partial coalescence of drops at liquid interfaces , Nature Phys. 2, 223 (2006).

[16] T. Gilet, K. Mulleners, J.P. Lecomte, N. Vandewalle, and S. Dorbolo, Critical parameters for the partial coalescence of a droplet, Phys. Rev. E 75, 036303 (2007).

[17] F. Blanchette, L. Messio, and J.W.M. Bush, The influence of surface tension gradients on drop coalescence, Phys. Fluids 21 (2009) 072107.

[18] S.T. Thoroddsen and K. Takehara, The coalescence cascade of a drop, Phys. Fluids 12, 1265 (2000).

[19] H. Aryafar and H.P. Kavehpour, Drop coalescence through planar surfaces, Phys. Fluids 18 072105 (2006).

[20] R. D. Deegan, P. Brunet, and J. Eggers, Complexities of splashing, Nonlinearity 21, C1 (2008).

[21] J. Hoepffner and G. Paré, Recoil of a liquid filament: escape from pinch-off through creation of a vortex ring, J. Fluid Mech. 734, 183 (2013).

[22] E. Ghabache, A. Antkowiak, C. Josserand, and T. Séon, On the physics of fizziness: How bubble bursting controls droplets ejection, Phys. Fluids 26, 121701 (2014).

[23] P. Walls, L. Henaux, and J. Bird, Jet drops from bursting bubbles: How gravity and viscosity couple to inhibit droplet production, Phys. Rev. E 92, 021002(R) (2015).

[24] M. Rieber and R. Frohn, A numerical study on the mechanism of splashing, Int. J. Heat Fluid Flow 20, 455 (1999).

[25] A. Gupta and R. Kumar, Two-Dimensional Lattice Boltzmann Model for Droplet Impingement and Breakup in Low Density Ratio Liquids, Commun. Comput. Phys. 10, pp. 767-784, (2011).

[26] E. Berberović, N.P. van Hinsberg, S. Jakirlic, I.V. Roisman, C. Tropea, Drop impact on to a liquid layer of finite thickness: dynamics of the cavity evolution, Phys. Rev. E 79, 036306 (2009).

[27] S. Chen and L. Guo, Viscosity Effect on regular bubble entrapment during drop impact into a deep pool, Chem. Eng. Sci. 109, 1 (2014).

[28] B. Ray, G. Biswas, and A. Sharma, Regimes during liquid drop impact on a liquid pool, J. Fluid Mech. 768, 492 (2015).

[29] A. Davanlou and R. Kumar, Thermally induced collision of droplets in an immiscible outer fluid, Sci. Rep. 5, 9531 (2015).

[30] A. Davanlou and R. Kumar, Counter-current motion of a droplet levitated on a liquid film undergoing Marangoni convection, Int. J. Heat Mass Transfer 89, 345 (2015).

[31] OpenFOAM Foundation, http://www.openfoam.org.

[32] R.I Issa, A.D Gosman, A.P Watkins, The computation of compressible and incompressible recirculating flows by a non-iterative implicit scheme, J. Comput. Phys. 62, 66 (1986).

[33] C.W. Hirt, B. D. Nichols, Volume of fluid (VOF) method for the dynamics of free boundaries, J. Comput. Phys. 39, 201 (1981).

[34] P. J. Pritchard, J.C. Leylegian, Fox and McDonalds's Introduction to Fluid Mechanics, 8th Edition, John Wiley & Sons, 2011.

[35] R. L. Panton, Incompressible Flow, 2nd Edition, John Wiley & Sons, New York, 1996.

[36] J.U. Brackbill, D.B. Kothe, C. Zemach, A continuum method for modeling surface tension, J. Comput. Phys. 100, 335 (1992).

[37] H.G. Weller, A New Approach to VOF-Based Interface Capturing Methods for Incompressible and Compressible Flow, OpenCFD Ltd, United Kingdom.

[38] E. Castillo-Orozco, A. Davanlou, P. Choudhury, and R. Kumar, Droplet impact on deep liquid pools: Rayleigh jet to formation of secondary droplets, Phys. Rev. E, (2015).

[39] J. Eggers, E. Villermaux, Physics of liquid jets, Rep. Prog. Phys. 71, 036601 (2008).

[40] P. Deepu, S. Basu, R. Kumar, Dynamics and fracture of ligaments from a droplet on a vibrating surface, Phys. Fluids 25, 082106 (2013).

[41] T. Tran, H. de Maleprade, C. Sun, D. Lohse, Air entrainment during impact of droplets on liquid surfaces, J. Fluid Mech. 726, R3 (2013).

[42] S. Chandrasekhar, Hydrodynamic and Hydromagnetic Stability, Oxford University Press, New York, 1961.

[43] L.E. Johns, R. Narayanan, Interfacial Instability, Springer, New York, 2002.